Journal of Computational Physics 529 (2025) 113892

Contents lists available at ScienceDirect

Journal of Computational Physics

journal homepage: www.elsevier.com/locate/jcp

An efficient compact splitting Fourier spectral method for computing the dynamics of rotating spin-orbit coupled spin-1 Bose-Einstein condensates

Xin Liu [a], Yongjun Yuan [b,*], Yong Zhang [a]

[a] Center for Applied Mathematics and KL-AAGDM, Tianjin University, Tianjin, 300072, China
[b] MOE-LCSM, School of Mathematics and Statistics, Hunan Normal University, Changsha, Hunan, 410081, China

ARTICLE INFO

Keywords:
Spin-1 Bose-Einstein condensates
Spin-orbit coupling
Rotating
Dynamics
Compact splitting

ABSTRACT

This paper focuses on the dynamic simulation of spin-1 Bose-Einstein condensates (BECs) with rotation and spin-orbit coupling (SOC), and presents a high-order compact splitting Fourier spectral method with favorable numerical properties. The Hamiltonian is split into a linear part, which consists of the Laplace, rotation and SOC terms, and a nonlinear part that includes all the remaining terms. The wave function is well approximated by the Fourier spectral method and is numerically accessed with discrete Fast Fourier transform (FFT). For the linear subproblem, we rotate the wave function by a function-rotation mapping, which is realized easily with purely FFT achieving almost optimal efficiency. The rotation term vanishes, but the SOC term becomes time-dependent. Using a time-dependent matrix decomposition and the function-rotation mapping, we can integrate the linear subproblem exactly and explicitly. The nonlinear subproblem is integrated analytically in physical space. Such "compact" splitting involves only two operators and facilitates the design of high-order splitting schemes. Our method is spectrally accurate in space and high order in time. It is efficient, explicit, unconditionally stable and simple to implement. In addition, we derive some dynamical properties and carry out a systematic study, including accuracy and efficiency tests, dynamical property verification, the SOC effects and dynamics of quantized vortices.

1. Introduction

Bose-Einstein condensation (BEC), first observed in 1995 [1,13], has provided a platform to study the macroscopic quantum world. In the early experiments, magnetic traps were used and the spin degrees of the atoms were then frozen. In 1998, by using an optical dipole trap, the internal spin degrees of freedom of a gas of spin-1 ^{23}Na atoms were liberated, and a spinor BEC was first produced [24]. Actually, in the optical trap, particles with different hyperfine states allow different angular momentum in space, resulting in a rich variety of spin texture. Recently, the spin-orbit coupling (SOC), which plays a key role in spin Hall effect, topological insulators [15], majorana fermions and spintronic devices [18], was successfully induced in experiments in a neutral atomic Bose-Einstein condensates by dressing two atomic spin states with a pair of lasers [20]. These experiments triggered a strong activity in the area of spin-orbit-coupled cold atoms. In particular, many investigations show that the combination of SOC, rotation

* Corresponding author.
E-mail addresses: liuxin_921@tju.edu.cn (X. Liu), yyj1983@hunnu.edu.cn (Y. Yuan), Zhang_Yong@tju.edu.cn (Y. Zhang).

https://doi.org/10.1016/j.jcp.2025.113892
Received 20 November 2024; Received in revised form 14 February 2025; Accepted 23 February 2025

Available online 25 February 2025

and atomic intrinsic interactions can generate various phenomena in the spinor BEC [16,19,31]. For example, a variety of exotic spin textures and fractional quantized vortices are exhibited for rotating spin-orbit-coupled BECs [32], a new necklace-type state with double-ring structure is created in a spin-1 BEC system due to the SOC and rotation, and the ground-state phase diagrams of the spin-orbit-angular-momentum coupled ^{87}Rb condensate are experimentally mapped out with first-order phase transitions [30].

At temperatures T much smaller than the critical temperature T_c, the properties of rotating spin-orbit coupled spin-1 BECs are well described by the macroscopic complex-valued wave function $\Psi = (\psi_1, \psi_0, \psi_{-1})^\top$ calculated from the three-dimensional (3D) coupled Gross-Pitaevskii equations (CGPEs) with an angular momentum term and spin-orbit coupling [3]. Moreover, the 3D CGPEs can be reduced to the effective two-dimensional (2D) equations if the external potential is highly anisotropic, i.e., much stronger in z-direction. In a unified way, the d-dimensional ($d = 2$ or $d = 3$) dimensionless CGPEs read as [31]

$$i\partial_t\psi_1(\mathbf{x},t) = \big[-\frac{1}{2}\Delta + V + c_0\rho - \Omega L_z\big]\psi_1 - \gamma L_0\psi_0 + c_1(\rho_0+\rho_1-\rho_{-1})\psi_1 + c_1\bar{\psi}_{-1}\psi_0^2, \tag{1.1}$$

$$i\partial_t\psi_0(\mathbf{x},t) = \big[-\frac{1}{2}\Delta + V + c_0\rho - \Omega L_z\big]\psi_0 - \gamma(L_0\psi_{-1} + L_1\psi_1) + c_1(\rho_1+\rho_{-1})\psi_0 + 2c_1\psi_1\psi_{-1}\bar{\psi}_0, \tag{1.2}$$

$$i\partial_t\psi_{-1}(\mathbf{x},t) = \big[-\frac{1}{2}\Delta + V + c_0\rho - \Omega L_z\big]\psi_{-1} - \gamma L_1\psi_0 + c_1(\rho_0+\rho_{-1}-\rho_1)\psi_{-1} + c_1\bar{\psi}_1\psi_0^2, \tag{1.3}$$

$$\psi_\ell(\mathbf{x},0) = \psi_\ell^0(\mathbf{x}), \quad \mathbf{x}\in\mathbb{R}^d, \quad \ell = 1,0,-1. \tag{1.4}$$

Here t denotes time and $\mathbf{x} = (x,y,z)^\top \in \mathbb{R}^3$ or $\mathbf{x} = (x,y)^\top \in \mathbb{R}^2$. The total density is given by $\rho = \rho_1 + \rho_0 + \rho_{-1}$, where $\rho_\ell = |\psi_\ell|^2$ represents the density of ℓ-th component. The constant Ω represents the angular velocity, and $L_z = -i(x\partial_y - y\partial_x)$ is the z-component of angular momentum. $L_0 = i\partial_x + \partial_y$ and $L_1 = i\partial_x - \partial_y$ are the spin-orbit coupling operators, and γ is the coupling strength. c_0 and c_1 are the dimensionless mean-field and interaction constants respectively. $\bar{f}$ denotes the conjugate of complex number f. $V(\mathbf{x})$ is a real-valued external trapping potential. In most BEC experiments, we choose a harmonic external trapping potential, i.e.,

$$V(\mathbf{x}) = \frac{1}{2}\begin{cases} \gamma_x^2x^2 + \gamma_y^2y^2, & d = 2, \\ \gamma_x^2x^2 + \gamma_y^2y^2 + \gamma_z^2z^2, & d = 3, \end{cases} \tag{1.5}$$

where the constant γ_υ ($\upsilon = x, y, z$) represents the trapping frequency in the υ-direction.

Introduce the spin-1 matrices $\mathbf{f} := (f_x, f_y, f_z)^\top$ as

$$f_x = \frac{1}{\sqrt{2}}\begin{pmatrix} 0 & 1 & 0 \\ 1 & 0 & 1 \\ 0 & 1 & 0 \end{pmatrix}, \quad f_y = \frac{i}{\sqrt{2}}\begin{pmatrix} 0 & -1 & 0 \\ 1 & 0 & -1 \\ 0 & 1 & 0 \end{pmatrix}, \quad f_z = \begin{pmatrix} 1 & 0 & 0 \\ 0 & 0 & 0 \\ 0 & 0 & -1 \end{pmatrix},$$

and the spin vector $\mathbf{F} := (F_x(\Psi), F_y(\Psi), F_z(\Psi))^\top := (\Psi^{\mathsf{H}} f_x \Psi, \Psi^{\mathsf{H}} f_y \Psi, \Psi^{\mathsf{H}} f_z \Psi)^\top$ (Ψ^{H} is the conjugate transpose of Ψ) of the condensate can be expressed as

$$\begin{aligned} F_x &= \frac{1}{\sqrt{2}}[\bar{\psi}_1\psi_0 + \bar{\psi}_0(\psi_1 + \psi_{-1}) + \bar{\psi}_{-1}\psi_0], \\ F_y &= \frac{i}{\sqrt{2}}[-\bar{\psi}_1\psi_0 + \bar{\psi}_0(\psi_1 - \psi_{-1}) + \bar{\psi}_{-1}\psi_0], \\ F_z &= |\psi_1|^2 - |\psi_{-1}|^2. \end{aligned}$$

Note that all spin-1 matrices are Hermitian and the spin vector entries are real numbers. The CGPEs (1.1)-(1.3) can be written in the following compact form

$$i\partial_t\Psi = \Big[(-\frac{1}{2}\Delta - \Omega L_z + V + c_0\rho)I_3 + c_1\mathbf{F}\cdot\mathbf{f} - \gamma S\Big]\Psi, \tag{1.6}$$

where I_3 is the 3×3 identity matrix and

$$\mathbf{F}\cdot\mathbf{f} = \begin{pmatrix} F_z & \frac{1}{\sqrt{2}}F_- & 0 \\ \frac{1}{\sqrt{2}}F_+ & 0 & \frac{1}{\sqrt{2}}F_- \\ 0 & \frac{1}{\sqrt{2}}F_+ & -F_z \end{pmatrix}, \qquad S = \begin{pmatrix} 0 & L_0 & 0 \\ L_1 & 0 & L_0 \\ 0 & L_1 & 0 \end{pmatrix},$$

with $F_+ = F_x + iF_y = \sqrt{2}(\bar{\psi}_1\psi_0 + \bar{\psi}_0\psi_{-1})$ and $F_- = F_x - iF_y = \bar{F}_+$.

There have been very extensive studies on the single-component BEC, most of which are concerned about the ground states computation and dynamics simulation, and we refer the readers to [2,4,6,7,12] for more details. For spinor BEC, the normalized gradient flow method [3,11] and time splitting spectral method [8] have been successfully applied to compute the ground states and dynamics respectively. While there are quite few literature on numerics for spinor BEC with SOC terms. As far as we known, the ground state has been studied for non-rotating spin-1 BEC [29], and it lacks research on dynamics simulation for the spinor BEC with SOC term and the more physically interesting rotating case. In this paper, we aim to carry out a comprehensive study of the dynamics for rotating spin-1 BEC with SOC.

Numerically, the most challenges lie in proper treatments of the rotation and SOC terms. Existing successful methods dealing with the rotating term include the alternating direction implicit (ADI) [7] method, rotating Lagrangian coordinates (RLC) method [6] and the exact splitting method (ESM) [10,21]. The standard ADI method splits the Hamiltonian into three parts and is of second order accurate in time. To effectively study fine structures existing in such rotating system, e.g., vortices lattice and/or vortex lines, it is favorable to adopt high-order numerical schemes. However, it is somewhat tedious and complicated to construct a high-order scheme with such triple operators. In ESM, the Laplace and rotation terms are grouped as a linear part, and the corresponding subproblem can be integrated analytically and explicitly in Fourier space [21], therefore, it is relatively easy to construct high order (temporal) scheme. But extension or adaptation of ESM to spin-1 BEC with SOC term is non-trivial and quite challenging. While in RLC, the rotation term automatically vanishes and it is simple to construct high-order schemes [6]. However, when real-time dynamics are required, it is imperative to rotate the wave function $\psi(\mathbf{x},t)$ from rotating Lagrangian coordinates to physical Cartesian coordinates at each time step t_n, and such rotation mapping is quite exhaustive computationally and poses great challenges to the simulation efficiency.

In practice, the rotation mapping is usually implemented using **Fourier spectral interpolation** and its computation boils down to a summation of Fourier series at **nonuniform** target grid $\mathcal{T}_{\mathrm{t}}$ using values given on **uniform** source grid $\mathcal{T}_{\mathrm{s}}$. Naive direct summation, whose complexity is $O(N^{d+2})$, becomes impractical for high dimensional problem due to its overwhelmingly huge computation costs and mediocre round-off performance. Even though the summation can be accelerated by NonUniform FFT (NUFFT) algorithm [22] with a significant reduction of complexity to $C\,N^d\log(N)$, the pre-factor C is super large and hinders any feasible efficiency performance. Therefore, an efficient numerical realization of the rotation mapping is of essential importance to overcome such efficiency bottleneck.

It is important to note that the target grid $\mathcal{T}_{\mathrm{t}}$ is exactly a rotation of the source grid $\mathcal{T}_{\mathrm{s}}$. Giving full consideration to the gird rotation shall help relieve the efficiency bottleneck. Fortunately, using three-shear decomposition of the rotation matrix [26] and its equivalent PDE reformulation (3.10), the rotation mapping can be reformulated into a computational-friendly form. We will refer to it as the *Rotation-Shear-Decomposition-Acceleration* (**RSDA**) method hereafter. Such idea has also been successfully applied to Vlasov-type equations [9]. Specifically, RSDA is composed of three simple differential operators, each of which takes the form of $e^{ay\partial_x}$ or $e^{bx\partial_y}$ with real constants a,b. It can be implemented efficiently with one-dimensional FFT/iFFT in Fourier space, thus leading to a significant efficiency enhancement.

To overcome such efficiency bottleneck, we introduce a high-order compact splitting Fourier spectral method. To be specific, the CGPEs (1.6) is split into a linear subproblem

$$i\partial_t\Psi(\mathbf{x},t)=\Big[(-\frac{1}{2}\Delta-\Omega L_z)I_3-\gamma S\Big]\Psi(\mathbf{x},t):=\mathcal{A}\Psi(\mathbf{x},t), \tag{1.7}$$

and a nonlinear subproblem

$$i\partial_t\Psi(\mathbf{x},t)=\Big[(V+c_0\rho)I_3+c_1\mathbf{F}\cdot\mathbf{f}\Big]\Psi(\mathbf{x},t):=\mathcal{B}\Psi(\mathbf{x},t). \tag{1.8}$$

The nonlinear subproblem is integrated analytically in physical space, while it seems difficult or even unlikely to integrate the linear subproblem in a similar way as before.

Borrowing the RLC idea to deal with the rotation term, we first rotate the wave function on the fixed rectangular domain, and such function-rotation can be implemented efficiently via purely FFT based on RSDA. For the rotated wave function, the rotation term vanishes but SOC term becomes time-dependent. Fortunately, we are able to integrate the linear system in Fourier space with help of a time-dependent matrix decomposition. We *do not* introduce or work in the rotating Lagrangian coordinates, instead, we just simply map the wave function by a rotation of spatial variables in the original coordinates. Therefore, the computation domain remains unchanged as a rectangle. It is worthy to emphasize that each subproblem can be efficiently and exactly solved in either Fourier or physical space, regardless of the potential $V(\mathbf{x})$. Such compact splitting greatly facilitates the implementation of high-order time marching schemes.

In summary, the key advance is that we first achieve fast and exact integration of the Laplace-Rotation-SOC subproblem using function-rotation mapping and a time-dependent matrix decomposition, where the mapping is efficiently computed with purely FFT instead of the commonly used NUFFT-accelerated Fourier spectral interpolation. Such fast realization of the function-rotation mapping is quite vital to alleviate or even overcome the efficiency bottleneck for simulating rotating models.

This paper is organized as follows. In Section 2, we derive some dynamical laws for some physical quantities. In Section 3, we propose an efficient and robust splitting Fourier spectral method to simulate the dynamics, and prove the mass conservation (unconditionally stability) and magnetization conservation. In Section 4, we test the temporal/spatial accuracies and efficiency, and study some interesting numerical phenomena. We make some concluding remarks in Section 5.

2. Dynamical properties

In this section, we demonstrate some main quantities in the study of dynamics of spin-1 BEC with rotation and SOC, including *mass, energy, magnetization, angular momentum expectation* and *condensate width*. The dynamical laws of these quantities are briefly presented and can be used as benchmarks for testing our numerical methods. Detailed proofs can be found in the appendixes.

Mass and energy. The time-dependent CGPEs (1.6) have two important invariants: the *mass* of the wave function and *the energy per particle*, i.e.,

$$\mathcal{N}(t) := \mathcal{N}(\Psi(\cdot,t)) := \int_{\mathbb{R}^d} \sum_{\ell=-1}^{1} \left|\psi_\ell(\mathbf{x},t)\right|^2 \mathrm{d}\mathbf{x} \equiv \mathcal{N}(\Psi(\cdot,0)) = 1, \quad t \geq 0, \tag{2.1}$$

and

$$\begin{aligned}\mathcal{E}(t) := \mathcal{E}(\Psi(\cdot,t)) := \int_{\mathbb{R}^d} \Bigg[& \sum_{\ell=-1}^{1} \left(\frac{1}{2}|\nabla\psi_\ell|^2 + V(\mathbf{x})|\psi_\ell|^2 - \Omega\bar{\psi}_\ell L_z\psi_\ell\right) \\ & + \frac{c_0}{2}\rho^2 + \frac{c_1}{2}\left(|F_+|^2 + |F_z|^2\right) \\ & - \gamma\left(L_0\psi_0\bar{\psi}_1 + L_0\psi_{-1}\bar{\psi}_0 + L_1\psi_1\bar{\psi}_0 + L_1\psi_0\bar{\psi}_{-1}\right)\Bigg] \mathrm{d}\mathbf{x} \\ \equiv\ & \mathcal{E}(\Psi(\cdot,0)).\end{aligned} \tag{2.2}$$

Magnetization. The *magnetization* of the wave function is defined as

$$\mathcal{M}(t) := \mathcal{M}(\Psi(\cdot,t)) := \sum_{\ell=-1}^{1} \int_{\mathbb{R}^d} \ell \left|\psi_\ell(\mathbf{x},t)\right|^2 \mathrm{d}\mathbf{x}, \quad t \geq 0. \tag{2.3}$$

By direct calculations, we obtain that the dynamics of the *magnetization* of the wave function is governed by

$$\frac{d}{dt}\mathcal{M}(t) = (2\gamma i)\mathfrak{R} \int_{\mathbb{R}^d} \left(\psi_1 L_1\bar{\psi}_0 - \bar{\psi}_{-1}L_1\psi_0\right)\mathrm{d}\mathbf{x}, \tag{2.4}$$

where $\mathfrak{R}$ represents the real part. This implies the *magnetization* is conserved (i.e., $\mathcal{M}(t) \equiv \mathcal{M}(0)$) when $\gamma = 0$.

Angular momentum expectation. The *angular momentum expectation* of the condensate (1.6) is defined as

$$\langle L_z\rangle(t) = \sum_{\ell=-1}^{1} \int_{\mathbb{R}^d} \bar{\psi}_\ell(\mathbf{x},t) L_z\psi_\ell(\mathbf{x},t)\mathrm{d}\mathbf{x}, \qquad t \geq 0. \tag{2.5}$$

The angular momentum expectation can be used to measure the vortex flux, and we have the following Lemma for its dynamics.

Lemma 1. *For CGPEs (1.6) with harmonic potential (1.5), the dynamics of angular momentum expectation is governed by the following ordinary differential equation (ODE)*

$$\frac{d\langle L_z\rangle(t)}{dt} = (\gamma_x^2 - \gamma_y^2)\int_{\mathbb{R}^d} xy\ \rho\ \mathrm{d}\mathbf{x} - 2\gamma\mathfrak{R}\int_{\mathbb{R}^d} i\left(\bar{\psi}_1 L_0\psi_0 - \bar{\psi}_{-1}L_1\psi_0\right)\mathrm{d}\mathbf{x}.$$

This demonstrates that the angular momentum expectation is conserved when $\gamma_x = \gamma_y$ and $\gamma = 0$. That is,

$$\langle L_z\rangle(t) \equiv \langle L_z\rangle(0), \qquad t \geq 0.$$

The detailed proof can be found in Appendix A.

Condensate width. The *condensate width* in the α-direction (where $\alpha = x, y, z$) is defined as $\sigma_\alpha = \sqrt{\delta_\alpha(t)}$, $t \geq 0$, where

$$\delta_\alpha(t) = \sum_{\ell=-1}^{1} \delta_{\alpha,\ell}(t) \qquad \text{with} \qquad \delta_{\alpha,\ell}(t) = \int_{\mathbb{R}^d} \alpha^2 \left|\psi_\ell(\mathbf{x},t)\right|^2 \mathrm{d}\mathbf{x}. \tag{2.6}$$

In particular, we have the following lemma for its dynamics in the 2D case.

Lemma 2. *For the 2D CGPEs (1.6) with the radially symmetric harmonic potential (1.5), i.e., $\gamma_x = \gamma_y =: \gamma_r$, it holds*

$$\frac{d^2\delta_r(t)}{dt^2} = -4\gamma_r^2\delta_r(t) + 4\mathcal{E}(0) + 4\Omega\langle L_z\rangle(t) + G(\gamma,\Psi), \tag{2.7}$$

where $\delta_r(t) := \delta_x(t) + \delta_y(t)$ and

$$G(\gamma,\Psi) = 4\gamma\mathfrak{R}\int_{\mathbb{R}^d} \left[\frac{\Omega}{\sqrt{2}}(ix+y)F_+ + \gamma\left(\rho + |\psi_0|^2 - \psi_1 L_z\bar{\psi}_1 + \psi_{-1}L_z\bar{\psi}_{-1}\right)\right]\mathrm{d}\mathbf{x}.$$

When $\gamma = 0$, it follows that

$$\delta_r(t) = \frac{\mathcal{E}(0) + \Omega\langle L_z\rangle(0)}{\gamma_r^2}\left[1 - \cos(2\gamma_r t)\right] + \delta_r^{(0)}\cos(2\gamma_r t) + \frac{\delta_r^{(1)}}{2\gamma_r}\sin(2\gamma_r t), \tag{2.8}$$

where $\delta_r^{(0)} = \delta_x(0) + \delta_y(0)$ *and* $\delta_r^{(1)} = \dot{\delta}_x(0) + \dot{\delta}_y(0)$. *Furthermore, if the initial condition is radically symmetric, we have*

$$\delta_x(t) = \delta_y(t) = \frac{1}{2}\delta_r(t), \quad t \geq 0.$$

In this case, the condensate widths $\sigma_x(t)$ *and* $\sigma_y(t)$ *are periodic functions with frequency that is twice the trapping frequency.*

Proof. See details in Appendix B. □

3. Numerical methods

The rotation and SOC terms bring challenges in simulating dynamics. A popular idea is to use the rotating Lagrangian coordinates to eliminate the rotation term [6]. Unfortunately, directly utilizing this idea poses efficiency challenges when real-time dynamics are required. Our approach splits the Hamiltonian into a linear part $\mathcal{A}$, (i.e., the *Laplace-Rotation-SOC* terms) and a nonlinear part $\mathcal{B}$, which contains the remaining terms. This splitting allows for a simple, exact and efficient evaluation of the nonlinear subproblem in physical space, since $\mathcal{B}(\Psi(\mathbf{x},t))$ is conserved. Remarkably, we develop an efficient and exact method for integrating the linear subproblem in Fourier space, with further details provided in subsection 3.1 below. Based on this, we can construct arbitrarily high-order time marching schemes.

To be exact, for a given time step $\tau > 0$, we define the time sequence as $t_n = n\tau$ for $n = 0, 1, \ldots$. Then from $t = t_n$ to t_{n+1}, we denote the solutions of linear and nonlinear subproblems as $\Psi(t) = e^{-i(t-t_n)\mathcal{A}}\Psi^n$ and $\Psi(t) = e^{-i(t-t_n)\mathcal{B}}\Psi^n$ respectively. In principle, high order splitting schemes can be constructed as [28]

$$\Psi^{n+1} = \left(\prod_{j=1}^{m} e^{-ia_j\tau\mathcal{A}} e^{-ib_j\tau\mathcal{B}}\right)\Psi^n,$$

where the coefficients $a_j, b_j \in \mathbb{C}$ are chosen suitably. For the classical second-order Strang splitting, we use $m = 2$, $a_1 = a_2 = \frac{1}{2}$ and $b_1 = 1$, $b_2 = 0$. For the fourth-order symplectic time integrator, we adopt $m = 4$, $a_1 = a_4 = \frac{1}{2(2-2^{1/3})}$, $a_2 = a_3 = \frac{1-2^{1/3}}{2(2-2^{1/3})}$ and $b_1 = b_3 = \frac{1}{2-2^{1/3}}$, $b_2 = -\frac{2^{1/3}}{2-2^{1/3}}$, $b_4 = 0$.

3.1. Exact integrator for the linear subproblem

In this subsection, we propose an exact and efficient integrator to solve

$$\begin{cases} i\partial_t\Psi(\mathbf{x},t) = \mathcal{A}\Psi(\mathbf{x},t), \quad t_n \leq t \leq t_{n+1}, \\ \Psi(\mathbf{x},t_n) = \Psi^n, \quad \mathbf{x} \in \mathbb{R}^d, \end{cases} \tag{3.1}$$

where $\mathcal{A}$ is the Laplace-Rotation-SOC operator given below

$$\mathcal{A} = (-\frac{1}{2}\Delta - \Omega L_z) I_3 - \gamma \begin{pmatrix} 0 & L_0 & 0 \\ L_1 & 0 & L_0 \\ 0 & L_1 & 0 \end{pmatrix}.$$

We define a **function-rotation mapping** through a rotation of variables, that is,

$$\phi_\ell(\mathbf{x},t) := \psi_\ell(\mathcal{R}(t)\mathbf{x},t), \quad \mathbf{x} \in \mathbb{R}^d,$$

where $\mathcal{R}(t)$ is a time-dependent rotational matrix and reads explicitly as

$$\mathcal{R}(t) = \begin{pmatrix} \cos(\Omega t) & \sin(\Omega t) \\ -\sin(\Omega t) & \cos(\Omega t) \end{pmatrix}, \text{ if } d = 2, \ \mathcal{R}(t) = \begin{pmatrix} \cos(\Omega t) & \sin(\Omega t) & 0 \\ -\sin(\Omega t) & \cos(\Omega t) & 0 \\ 0 & 0 & 1 \end{pmatrix}, \text{ if } d = 3. \tag{3.2}$$

Using the chain rule, for the rotated-function $\Phi = (\phi_1, \phi_0, \phi_{-1})^\top$, we have

$$\begin{cases} i\partial_t\Phi(\mathbf{x},t) = \widetilde{\mathcal{A}}(t)\Phi(\mathbf{x},t), \quad t_n \leq t \leq t_{n+1}, \\ \Phi(\mathbf{x},t_n) = \Psi(\mathcal{R}(t_n)\mathbf{x},t_n) := \Phi^n, \quad \mathbf{x} \in \mathbb{R}^d, \end{cases} \tag{3.3}$$

where

$$\widetilde{\mathcal{A}} = (-\frac{1}{2}\Delta)\ I_3 - \gamma \begin{pmatrix} 0 & \widetilde{L}_0 & 0 \\ \widetilde{L}_1 & 0 & \widetilde{L}_0 \\ 0 & \widetilde{L}_1 & 0 \end{pmatrix}$$

with

$$\widetilde{L}_0 = i\left[\cos(\Omega t)\partial_x + \sin(\Omega t)\partial_y\right] + \left[-\sin(\Omega t)\partial_x + \cos(\Omega t)\partial_y\right],$$
$$\widetilde{L}_1 = i\left[\cos(\Omega t)\partial_x + \sin(\Omega t)\partial_y\right] - \left[-\sin(\Omega t)\partial_x + \cos(\Omega t)\partial_y\right].$$

Clearly, the Laplace keep unchanged but the SOC terms are time-dependent.

Since the wave function ψ_ℓ is smooth and decays exponentially fast, its rotated function ϕ_ℓ is also smooth and decays fast. Therefore, it is reasonable to truncate the whole space $\mathbb{R}^d$ into a common large enough bounded domain $\mathcal{D} = [-L, L]^d,\ L > 0$ and impose periodic boundary conditions for both ψ_ℓ and ϕ_ℓ. Then we can readily apply the Fourier spectral method [23] to approximate both wave functions and their spatial derivatives.

It is crucial to calculate function-rotation mapping accurately and efficiently. Based on matrix decomposition and PDE reformulation, we introduce a strategy (RSDA) to calculate this mapping with almost optimal efficiency, which only requires one-dimensional FFT. That is,

$$\begin{aligned}
\phi_\ell^n(\mathbf{x}) &= e^{a_1 y\partial_x} e^{b_1 x\partial_y} e^{a_1 y\partial_x} \psi_\ell^n(\mathbf{x}), \quad \mathbf{x} \in \mathbb{R}^d, \\
\psi_\ell^{n+1}(\mathbf{x}) &= e^{a_2 y\partial_x} e^{b_2 x\partial_y} e^{a_2 y\partial_x} \phi_\ell^{n+1}(\mathbf{x}), \quad \mathbf{x} \in \mathbb{R}^d,
\end{aligned}$$

where $a_1 = \tan(\Omega t_n/2)$, $b_1 = -\sin(\Omega t_n)$, $a_2 = -\tan(\Omega t_{n+1}/2)$ and $b_2 = \sin(\Omega t_{n+1})$. Further details are provided in subsection 3.1.2.

Remark 3.1. We do not work in the rotating Lagrangian coordinates, but just simply rotate the wave functions and compute them on a fixed rectangular domain in the original Cartesian coordinates. Such function-rotation can be implemented via purely FFT based on RSDA.

Specifically, we shall introduce our method in 2D and choose to discretize domain $\mathcal{D}$ with uniform mesh size $h = (2L)/N, N \in 2Z^+$. For simplicity, we define the Fourier, physical index and grid points sets as

$$\begin{aligned}
\mathcal{T}_N &= \left\{ (p,q) \in \mathbb{Z}^2 \,\middle|\, -N/2 \le p \le N/2-1,\ -N/2 \le q \le N/2-1 \right\}, \\
\mathcal{I}_N &= \left\{ (j,k) \in \mathbb{Z}^2 \,\middle|\, 0 \le j \le N-1,\ 0 \le k \le N-1 \right\}, \\
\mathcal{G} &= \left\{ \mathbf{x}_{jk} := (x_j, y_k)^\top := (-L + jh, -L + kh)^\top, \quad (j,k) \in \mathcal{I}_N \right\},
\end{aligned}$$

and define $\psi_{\ell,jk}^n (\ell = 1, 0, -1)$ as the computational approximation of $\psi_\ell(x_j, y_k, t_n)$ for $(j,k) \in \mathcal{I}_N,\ n > 0$. In order to discrete (3.3), we approximate the function ϕ_ℓ by applying the Fourier spectral method

$$\phi_\ell(x,y,t) \approx \sum_{(p,q)\in\mathcal{T}_N} \widehat{\phi}_{\ell,pq}(t)\, e^{i\nu_p^x (x+L)} e^{i\nu_q^y (y+L)}, \quad (x,y) \in \mathcal{D},$$

where $\nu_p^x = 2\pi p/(2L)$, $\nu_q^y = 2\pi q/(2L)$. The discrete Fourier coefficients are presented as follows

$$\widehat{\phi}_{\ell,pq}(t) = \frac{1}{N^2} \sum_{(j,k)\in\mathcal{I}_N} \phi_\ell(x_j, y_k, t)\, e^{-i\nu_p^x (x_j+L)} e^{-i\nu_q^y (y_k+L)}, \quad (p,q) \in \mathcal{T}_N. \tag{3.4}$$

Using the Fourier spectral approximation in space, the semi-discretization of (3.3) can be written in terms of the Fourier coefficients as

$$\begin{cases}
i\partial_t \widehat{\Phi}_{pq}(t) = A(t)\widehat{\Phi}_{pq}(t), & t_n \le t \le t_{n+1}, \\
\widehat{\Phi}_{pq}(t_n) = (\widehat{\Phi^n})_{pq}, & (p,q) \in \mathcal{T}_N,
\end{cases} \tag{3.5}$$

with $\widehat{\Phi}_{pq} := (\widehat{\phi}_{1,pq},\ \widehat{\phi}_{0,pq},\ \widehat{\phi}_{-1,pq})^\top$. The time-dependent coefficient matrix reads as

$$A(t) = \frac{1}{2}\left[(\nu_p^x)^2 + (\nu_q^y)^2 \right] I_3 - \gamma R(t),$$

where $R = \begin{pmatrix} 0 & \alpha & 0 \\ \bar{\alpha} & 0 & \alpha \\ 0 & \bar{\alpha} & 0 \end{pmatrix}$ with $\alpha(t) = -\left[\cos(\Omega t)\nu_p^x + \sin(\Omega t)\nu_q^y\right] + i\left[-\sin(\Omega t)\nu_p^x + \cos(\Omega t)\nu_q^y\right]$. With an abuse of notations, we shall omit the subscripts p and q for simplicity. We introduce a new vector

$$K(t) := e^{\frac{1}{2} i[(\nu_p^x)^2 + (\nu_q^y)^2](t-t_n)}\, \widehat{\Phi}_{pq}(t) \in \mathbb{C}^{3\times 1},$$

and it satisfies the following ODE system

$$\partial_t K(t) = i\gamma R(t) K(t), \quad \text{with} \quad K(t_n) = (\widehat{\Phi^n})_{pq}. \tag{3.6}$$

In fact, the above equation can be integrated *exactly* by virtue of a time-dependent matrix eigenvector decomposition and we shall present details in the coming subsection.

3.1.1. Exact temporal integration

In this subsection, we aim to integrate equation (3.6). Similar to the diagonalization procedure, we first carry out an eigenvector decomposition of matrix R, then convert (3.6) to a *constant* coefficient linear ODE system. Actually, we can diagonalize R explicitly using a unitary matrix U (i.e., $UU^{\mathsf{H}} = U^{\mathsf{H}}U = I_3$) to a real diagonal matrix Λ such that $R = U\Lambda U^{\mathsf{H}}$. That is,

$$U=\begin{pmatrix} \frac{\alpha}{\sqrt{2}|\alpha|} & \frac{\alpha}{2|\alpha|} & \frac{\alpha}{2|\alpha|} \\ 0 & \frac{1}{\sqrt{2}} & -\frac{1}{\sqrt{2}} \\ \frac{-\bar{\alpha}}{\sqrt{2}|\alpha|} & \frac{\bar{\alpha}}{2|\alpha|} & \frac{\bar{\alpha}}{2|\alpha|} \end{pmatrix}, \quad \Lambda=\begin{pmatrix} 0 & 0 & 0 \\ 0 & \sqrt{2}|\alpha| & 0 \\ 0 & 0 & -\sqrt{2}|\alpha| \end{pmatrix}.$$

We perform a time-dependent variable transformation $Z(t) := U^{\mathsf{H}}(t)K(t)$, and then we have

$$\begin{cases} \partial_t Z = \partial_t(U^{\mathsf{H}})K + U^{\mathsf{H}}(\partial_t K) = i\left[\Omega G + \gamma\Lambda\right] Z, \\ Z(t_n) = U^{\mathsf{H}}(t_n)K(t_n), \end{cases} \tag{3.7}$$

where the *constant* coefficient matrix $G = \frac{-1}{\sqrt{2}}\begin{pmatrix} 0 & 1 & 1 \\ 1 & 0 & 0 \\ 1 & 0 & 0 \end{pmatrix}$. Since $|\alpha| = \sqrt{(v_p^x)^2 + (v_q^y)^2}$ is time-independent, equation (3.7) is actually an ODE system with *constant* skew-Hermitian coefficient matrix. Then we have

$$Z(t) = e^{i[\Omega G+\gamma\Lambda](t-t_n)} Z(t_n).$$

Correspondingly, the solution to equation (3.6) is

$$K(t) = U(t)Z(t) = \left[U(t)e^{i[\Omega G+\gamma\Lambda](t-t_n)}U^{\mathsf{H}}(t_n)\right]K(t_n) := W(t)K(t_n),$$

where $W(t)$ is a unity matrix and reads explicitly as follows

$$W(t) = \begin{pmatrix} \alpha\bar{\alpha}_n c_{11} & \alpha c_{12} & \alpha\alpha_n c_{13} \\ \bar{\alpha}_n c_{12} & c_{22} & \alpha_n c_{23} \\ \bar{\alpha}\bar{\alpha}_n c_{13} & \bar{\alpha}c_{23} & \bar{\alpha}\alpha_n c_{33} \end{pmatrix}, \tag{3.8}$$

with entries

$$c_{11} = \frac{1}{4\lambda^2|\alpha|^2}\left[2\lambda^2(\eta_1+2) - \xi^2\eta_1 - 2\Omega\lambda\eta_2\right], \qquad c_{12} = \frac{\gamma}{2\lambda^2}\left[-\Omega\eta_1 + \lambda\eta_2\right],$$
$$c_{13} = \frac{\gamma^2\eta_1}{2\lambda^2}, \qquad c_{22} = 1 + \frac{\xi^2\eta_1}{2\lambda^2}, \qquad c_{23} = c_{12} + \frac{\gamma\Omega\eta_1}{\lambda^2}, \qquad c_{33} = c_{11} + \frac{\Omega\eta_2}{\lambda|\alpha|^2},$$

where $\xi = \sqrt{2}\gamma|\alpha|$, $\lambda = \sqrt{\xi^2+\Omega^2}$, $\eta_1 = 2\cos(\lambda(t-t_n)) - 2$, $\eta_2 = 2i\sin(\lambda(t-t_n))$. Notice that parameters $c_{11}, c_{12}, c_{13}, c_{22}, c_{23}$ and c_{33} depend only on γ, Ω and the time step τ, hence they can be computed once and treated as a pre-computation.

Therefore, the exact solution to (3.5) reads as follows

$$\widehat{\Phi}_{pq}(t) = e^{-\frac{1}{2}i[(v_p^x)^2+(v_q^y)^2](t-t_n)}K(t) = e^{-\frac{1}{2}i[(v_p^x)^2+(v_q^y)^2](t-t_n)}W(t)(\widehat{\Phi^n})_{pq}.$$

Then, we have

$$\boxed{\Phi_{jk}^{n+1} = \sum_{(p,q)\in\mathcal{T}_N} e^{-\frac{1}{2}i[(v_p^x)^2+(v_q^y)^2]\tau}\, W(t_{n+1})\,(\widehat{\Phi^n})_{pq}\, e^{iv_p^x(x_j+L)}e^{iv_q^y(y_k+L)}.} \tag{3.9}$$

Finally, we obtain the solution to (3.1) as

$$\psi_\ell^{n+1}(\mathbf{x}_{jk}) = \phi_\ell^{n+1}(\mathcal{R}^{-1}(t_{n+1})\mathbf{x}_{jk}) \quad \text{with} \quad \mathbf{x}_{jk} = (x_j, y_k)^\top.$$

Remark 3.2 *(Special cases)*. The above method naturally resolves special physical cases, including the vanishing spin-orbit coupling case ($\gamma = 0$) and/or the non-rotating case ($\Omega = 0$).

- **Non-SOC**: When the spin-orbit coupling strength γ goes to zero, for any fixed rotating speed Ω, we have $W(t) \to I_3$ as $\gamma \to 0$, and the numerical scheme (3.9) reads as follows

  $$\Phi_{jk}^{n+1} = \sum_{(p,q)\in\mathcal{T}_N} e^{-\frac{1}{2}i[(v_p^x)^2+(v_q^y)^2]\tau}(\widehat{\Phi^n})_{pq}\, e^{iv_p^x(x_j+L)}e^{iv_q^y(y_k+L)}.$$

  Obviously, this scheme aligns with the numerical scheme for solving the PDEs (3.3) with $\gamma = 0$ (i.e., $\widetilde{\mathcal{A}} = (-\frac{1}{2}\Delta)\, I_3$).
- **Non-rotating**: When the rotating speed Ω goes to zero, simple calculations imply that

  $$W(t) \longrightarrow e^{i\gamma R(t-t_n)}, \quad \text{as} \quad \Omega \to 0.$$

  Similarly, the corresponding numerical scheme aligns with the scheme for solving the PDEs (3.1) with $\Omega = 0$ (i.e., $\mathcal{A} = (-\frac{1}{2}\Delta)\, I_3 - \gamma S$).

Remark 3.3 *(Extension to three dimensional problem).* It is straightforward to extend the above method to three dimensional case, because both the rotation and SOC terms are independent of space variable z, and we choose to omit details for brevity.

3.1.2. Fast implementation of the function-rotation mapping

To ensure that the proposed procedure is computationally viable, we present a specific scheme (RSDA) for the following problems

$$\begin{aligned}&\text{given}\quad \psi_\ell^n(\mathbf{x}_{jk}) \quad\Longrightarrow\quad \text{compute}\quad \phi_\ell^n(\mathbf{x}_{jk}) = \psi_\ell^n(\mathcal{R}(t_n)\mathbf{x}_{jk}),\quad \mathbf{x}_{jk}\in\mathcal{G},\\ &\text{given}\ \phi_\ell^{n+1}(\mathbf{x}_{jk}) \quad\Longrightarrow\quad \text{compute}\quad \psi_\ell^{n+1}(\mathbf{x}_{jk}) = \phi_\ell^{n+1}(\mathcal{R}^{-1}(t_{n+1})\mathbf{x}_{jk}),\quad \mathbf{x}_{jk}\in\mathcal{G}.\end{aligned}$$

The numerical problem is to compute the function ϕ_ℓ^n on the uniform grid $\mathbf{x}_{jk}$ using discrete values of ψ_ℓ^n on the same uniform grid $\mathbf{x}_{jk}$.

Based on a three-shear decomposition of a rotation matrix [26], and the equivalent PDE reformulation (3.10), the function-rotation mapping can be reformulated exactly into a computational-friendly form, which is easy to implement with purely one-dimensional FFT and iFFT achieving almost optimal efficiency. To be specific, the rotation matrix (3.2) can be reformulated as $\mathcal{R}(t) = e^{t\Omega J}$ with the second order symplectic matrix $J := \left(\begin{smallmatrix}0 & 1\\ -1 & 0\end{smallmatrix}\right)$ if $d=2$ and $J := \left(\begin{smallmatrix}0 & 1 & 0\\ -1 & 0 & 0\\ 0 & 0 & 0\end{smallmatrix}\right)$ if $d=3$.

In fact, for any given $d\times d$ matrix M, we can prove that the following identity holds true

$$u(e^{tM}\mathbf{x}) = e^{tM\mathbf{x}\cdot\nabla}u(\mathbf{x}),\qquad \mathbf{x}\in\mathbb{R}^d, \tag{3.10}$$

because both the left-hand side (LHS) and the right-hand side (RHS) of (3.10) are exact solutions to the underlying transport equation

$$\begin{cases}\partial_t w = M\mathbf{x}\cdot\nabla w, & \mathbf{x}\in\mathbb{R}^d,\\ w(t=0,\mathbf{x}) = u(\mathbf{x}).\end{cases}$$

However, one *can not* directly apply the above formula (3.10) to calculate the function-rotation mapping simply because $J\mathbf{x}\cdot\nabla$ has *non*-constant coefficients. Thanks to the three-shear decomposition of a rotation matrix, that is,

$$\mathcal{R}(t) = e^{M_1(t)}e^{M_2(t)}e^{M_1(t)},\qquad \Omega t\neq(2k+1)\pi,\ k\in\mathbb{Z}^+, \tag{3.11}$$

where M_1, M_2 are nilpotent matrices and read explicitly as

$$M_1(t) = \begin{pmatrix}0 & \tan(\frac{\Omega t}{2})\\ 0 & 0\end{pmatrix},\quad M_2(t) = \begin{pmatrix}0 & 0\\ -\sin(\Omega t) & 0\end{pmatrix}\quad\text{if}\quad d=2,$$

and

$$M_1(t) = \begin{pmatrix}0 & \tan(\frac{\Omega t}{2}) & 0\\ 0 & 0 & 0\\ 0 & 0 & 0\end{pmatrix},\quad M_2(t) = \begin{pmatrix}0 & 0 & 0\\ -\sin(\Omega t) & 0 & 0\\ 0 & 0 & 0\end{pmatrix}\quad\text{if}\quad d=3,$$

we have

$$\begin{aligned}\phi_\ell^n(\mathbf{x}) &= \psi_l^n(e^{M_1(t_n)}e^{M_2(t_n)}e^{M_1(t_n)}\mathbf{x}) = e^{M_1(t_n)\mathbf{x}\cdot\nabla}\psi_l^n(e^{M_1(t_n)}e^{M_2(t_n)}\mathbf{x})\\ &= e^{M_1(t_n)\mathbf{x}\cdot\nabla}e^{M_2(t_n)\mathbf{x}\cdot\nabla}\psi_l^n(e^{M_1(t_n)}\mathbf{x}) = e^{M_1(t_n)\mathbf{x}\cdot\nabla}e^{M_2(t_n)\mathbf{x}\cdot\nabla}e^{M_1(t_n)\mathbf{x}\cdot\nabla}\psi_\ell^n(\mathbf{x})\\ &= e^{a_1y\partial_x}e^{b_1x\partial_y}e^{a_1y\partial_x}\psi_\ell^n(\mathbf{x}),\end{aligned} \tag{3.12}$$

where $a_1 = \tan(\Omega t_n/2)$, $b_1 = -\sin(\Omega t_n)$. Similarly, we obtain

$$\psi_\ell^{n+1}(\mathbf{x}) = e^{a_2y\partial_x}e^{b_2x\partial_y}e^{a_2y\partial_x}\phi_\ell^{n+1}(\mathbf{x}), \tag{3.13}$$

where $a_2 = -\tan(\Omega t_{n+1}/2)$, $b_2 = \sin(\Omega t_{n+1})$. To sum up, the **RSDA** method for fast evaluation of the function-rotation mapping reads as follows

$$\boxed{\begin{aligned}\phi_\ell^n(\mathbf{x}) &= e^{a_1y\partial_x}e^{b_1x\partial_y}e^{a_1y\partial_x}\psi_\ell^n(\mathbf{x}),\\ \psi_\ell^{n+1}(\mathbf{x}) &= e^{a_2y\partial_x}e^{b_2x\partial_y}e^{a_2y\partial_x}\phi_\ell^{n+1}(\mathbf{x}).\end{aligned}}$$

Remark 3.4. If $\Omega t = (2k+1)\pi$, the entry $\tan(\Omega t/2)$ in the matrix $M_1(t)$ is not well-defined. In such particular case, to realize the function mapping, we do not perform decomposition as shown in Eqn. (3.11). Actually, the function-rotating mapping is exactly the reflection operation over the origin, and one can easily realize such mapping by flipping the function against the x and y-axis successively.

We discrete (3.12)-(3.13) in space by Fourier spectral method [23], taking (3.12) as an example, and the specific discretization scheme is given below

Table 1
The performance of RSDA and NUFFT for function-rotation mapping evaluation in Example 1.

$N = 256$	2D		3D	
	Error	Time	Error	Time
RSDA	6.9459E-16	0.012	6.9459E-16	2.66
NUFFT	1.3545E-14	0.171	1.3545E-14	48.25

$$\begin{aligned}
\phi^{(1)}_{\ell}(x_j, y_k) &= \sum_{p=-N/2}^{N/2-1} e^{a_1 y_k (iv_p^x)} \left(\widehat{\psi^n_{\ell}(\cdot, y_k)}\right)_p e^{iv_p^x (x_j + L)}, \\
\phi^{(2)}_{\ell}(x_j, y_k) &= \sum_{q=-N/2}^{N/2-1} e^{b_1 x_j (iv_q^y)} \left(\widehat{\phi^{(1)}_{\ell}(x_j, \cdot)}\right)_q e^{iv_q^y (y_k + L)}, \\
\phi^{n}_{\ell}(x_j, y_k) &= \sum_{p=-N/2}^{N/2-1} e^{a_1 y_k (iv_p^x)} \left(\widehat{\phi^{(2)}_{\ell}(\cdot, y_k)}\right)_p e^{iv_p^x (x_j + L)}.
\end{aligned} \tag{3.14}$$

Here, $\widehat{f}_p$ and $\widehat{f}_q$ represent the discrete Fourier transform coefficients of the vector f in x- and y-directions, respectively.

In the following, we will demonstrate the efficiency and accuracy of RSDA method for function-rotation mapping evaluation and compare it with Fourier spectral interpolation, that is,

$$\phi^n_{\ell}(x_j, y_k) \approx \sum_{(p,q)\in\mathcal{I}_N} \widehat{\psi}^n_{\ell,pq}\, e^{iv_p^x(\cos(\Omega t_n)x_j + \sin(\Omega t)y_k + L)} e^{iv_q^y(-\sin(\Omega t_n)x_j + \cos(\Omega t)y_k + L)},$$

with the discrete Fourier coefficients $\widehat{\psi}^n_{\ell,pq}$ being given as (3.4). This interpolation boils down to a summation of Fourier series at nonuniform grid. Note that the approximation only needs to be done in the x- and y-directions for 3D problem, because the rotation is independent of the space variable z. Therefore, the complexity of naive direct summation is $\mathcal{O}(N^{d+2})$. The NUFFT-accelerated algorithm requires N^{d-2} **two-dimensional** FFT and NUFFT algorithm to accelerate the Fourier spectral interpolation, whose complexity is reduced to $C\,N^d \log(N)$ with a super large pre-factor C [14,22]. The RSDA method only needs $3N^{d-1}$ pairs of **one-dimensional** FFT and iFFT, thus achieving almost optimal efficiency.

Example 1 *(Numerical performance).* Here, we choose $\Omega = 0.6$, $t_n = 1$, and

$$\psi^n(\mathbf{x}) = \begin{cases} (x+iy)e^{-(x+0.1)^2-(y-0.3)^2}, & d = 2, \\ (x+iy)e^{-(x+0.1)^2-(y-0.3)^2-z^2}, & d = 3. \end{cases}$$

Then we have $\phi^n(\mathbf{x}) = \psi^n(\mathcal{R}(t_n)\mathbf{x})$. In our simulation, we compare the accuracy and efficiency of RSDA (3.14) and Fourier spectral interpolation accelerated with NUFFT algorithm [14,22] to evaluate $\phi^n(\mathbf{x})$. The algorithms were implemented in Matlab (2022a) and run on a 1.60GH Intel(R) Core(TM) i5-8265U CPU with a 6 MB cache in Windows.

Table 1 presents the relative maximum error and computational time (in seconds) for RSDA and NUFFT-accelerated spectral interpolation algorithm with $h = 1/8$ on domain $\mathcal{D} = [-16, 16]^d$. From this, we can conclude that RSDA method performs better in terms of efficiency and accuracy.

To sum up, from time t_n to t_{n+1}, we can solve the linear problem using the following exact integrator.

Algorithm 1 Exact integrator for the linear subproblem.

Input: Given $\psi^n_{\ell,jk} := \psi^n_{\ell}(\mathbf{x}_{jk})$.

1: Compute the function-rotation mapping $\phi^n_{\ell,jk} = \psi^n_{\ell}(\mathcal{R}(t_n)\mathbf{x}_{jk})$ by (3.14).

2: Solve the ODEs (3.3) to obtain $\phi^{n+1}_{\ell}(\mathbf{x}_{jk})$ using (3.9).

3: Compute the function-rotation mapping $\psi^{n+1}_{\ell,jk} = \phi^{n+1}_{\ell}(\mathcal{R}^{-1}(t_{n+1})\mathbf{x}_{jk})$ by (3.13).

Remark 3.5 *(Efficiency).* For Algorithm 1, it appears that we need $\mathbf{8N}$ pairs of one-dimensional FFT and iFFT. In fact, we can reduce the number of Fourier-Physical switches by merging adjacent computation. To be specific, at the end of step 1, we do not perform the inverse Fourier transform in x-direction but stay in phase space, because the subsequent computation is carried out in Fourier space with respect to x- and y-directions. This strategy helps reduce N pairs of one-dimensional FFT and iFFT. Similarly, we can save another N pairs of one-dimensional FFT and iFFT from steps 2 to 3. Therefore, it requires only $\mathbf{6N}$ pairs of **one-dimensional** FFT and iFFT, and the complexity is $\mathcal{O}(N^2 \log(N))$.

Similarly, for 3D problem, we need $\mathbf{7N^2}$ pairs of one-dimensional FFT and iFFT, and the complexity is $\mathcal{O}(N^3 \log(N))$.

3.2. Exact integrator for the nonlinear subproblem

In this subsection, as referenced in [3,25], we present an exact solution to the following nonlinear problem

$$\begin{cases} i\partial_t \Psi(\mathbf{x},t) = \big[(V + c_0\rho)I_3 + c_1\mathbf{F}\cdot\mathbf{f}\big]\Psi(\mathbf{x},t) := \mathcal{B}\Psi(\mathbf{x},t), \\ \Psi(\mathbf{x},t_n) = \Psi^n, \quad \mathbf{x}\in\mathcal{D}, \quad t_n \le t \le t_{n+1}. \end{cases} \tag{3.15}$$

We prove that the density ρ is time-invariant, i.e., $\rho(\mathbf{x},t)\equiv\rho(\mathbf{x},t_n) := \rho^n$ for any time $t_n \le t \le t_{n+1}$. Using the facts that $f_v (v = x, y, z)$ and $\mathcal{B}$ are Hermitian matrices, and that the commutator relations $[f_x, f_y] := f_x f_y - f_y f_x = i f_z$, $[f_y, f_z] = i f_x$, and $[f_z, f_x] = i f_y$ hold, we have

$$\begin{aligned} \partial_t F_v &= \partial_t(\Psi^{\mathsf{H}} f_v \Psi) = i\Psi^{\mathsf{H}}\mathcal{B} f_v \Psi - i\Psi^{\mathsf{H}} f_v \mathcal{B}\Psi \\ &= ic_1\Psi^{\mathsf{H}}[\mathbf{F}\cdot\mathbf{f}, f_v]\Psi \;=\; ic_1\Psi^{\mathsf{H}}[F_x f_x + F_y f_y + F_z f_z, f_v]\Psi \\ &= ic_1\big(F_x\Psi^{\mathsf{H}}[f_x, f_v]\Psi + F_y\Psi^{\mathsf{H}}[f_y, f_v]\Psi + F_z\Psi^{\mathsf{H}}[f_z, f_v]\Psi\big) = 0, \quad v = x, y, z. \end{aligned}$$

This implies that the spin vector $F_v(\Psi(t)) \equiv F_v(\Psi^n)$ and $\mathcal{B}(\Psi(t)) \equiv \mathcal{B}(\Psi^n) := \mathcal{B}^n$, $\forall\, t_n \le t \le t_{n+1}$. It is clear that (3.15) becomes a linear ODE and the exact solution reads as follows

$$\Psi(\mathbf{x},t) = e^{-i(t-t_n)\mathcal{B}^n}\Psi^n = e^{-i(t-t_n)(V+c_0\rho^n)}e^{-ic_1(t-t_n)\mathbf{F}^n\cdot\mathbf{f}}\Psi^n, \tag{3.16}$$

where $\mathbf{F}^n = (F_x^n, F_y^n, F_z^n)^\top$. The eigenvalues of $\mathbf{F}^n\cdot\mathbf{f}$ are $|\mathbf{F}^n|, -|\mathbf{F}^n|$ and 0. The associated eigenvectors are e_1^n, e_2^n and $e_3^n = |\mathbf{F}^n|^{-1}2^{-\frac{1}{2}}(-F_-^n, \sqrt{2}F_z^n, F_+^n)^\top$. In fact, we can expand the wave function vector Ψ^n with respect to the above eigenvectors as $\Psi^n = l_1 e_1^n + l_2 e_2^n + l_3 e_3^n$. It is easy to prove that $l_3 = \langle\Psi^n, e_3^n\rangle = 0$ by substituting the explicit formula of e_3^n as follows

$$\begin{aligned} l_3 &= \langle\Psi^n, e_3^n\rangle = |\mathbf{F}^n|^{-1}(-\psi_1^n F_+^n/\sqrt{2} + \psi_0^n F_z^n + \psi_{-1}^n F_-^n/\sqrt{2}) \\ &= |\mathbf{F}^n|^{-1}\big(-\psi_1^n(\bar{\psi}_1^n\psi_0^n + \bar{\psi}_0^n\psi_{-1}^n) + \psi_0^n(|\psi_1^n|^2 - |\psi_{-1}^n|^2) + \psi_{-1}^n(\psi_1^n\bar{\psi}_0^n + \psi_0^n\bar{\psi}_{-1}^n)\big) \\ &= 0. \end{aligned}$$

Then we have

$$(\mathbf{F}^n\cdot\mathbf{f})^2\Psi^n = (\mathbf{F}^n\cdot\mathbf{f})^2(l_1 e_1^n + l_2 e_2^n) = |\mathbf{F}^n|^2(l_1 e_1^n + l_2 e_2^n) = |\mathbf{F}^n|^2\Psi^n,$$

and the solution (3.16) can be computed as

$$\Psi(\mathbf{x},t) = e^{-i(t-t_n)(V+c_0\rho^n)}\left[\cos(c_1(t-t_n)|\mathbf{F}^n|)\Psi^n - i\frac{\sin(c_1(t-t_n)|\mathbf{F}^n|)}{|\mathbf{F}^n|}(\mathbf{F}^n\cdot\mathbf{f})\Psi^n\right]. \tag{3.17}$$

In practice, from time $t = t_n$ to $t = t_{n+1}$, we combine the splitting steps via the standard Strang splitting and present detailed step-by-step algorithm proposed in Algorithm 2.

Algorithm 2 Second-order compact splitting Fourier spectral method.

1: Solve ODEs (3.15) by (3.17) for half time step $\tau/2$ with initial data given at $t = t_n$.
2: Solve ODEs (3.1) by Algorithm 1 for one step τ starting with the data obtained from step 1.
3: Solve ODEs (3.15) by (3.17) for half time step $\tau/2$ again with the data acquired from step 2.

Remark 3.6 *(Arbitrary high-order schemes).* We can easily design high-order schemes using the operator splitting method [28] since both subproblems can be exactly integrated.

3.3. Stability

Without loss of generality, we only present proofs in the 2D case and extension to 3D is straightforward. We define the discrete l^2-norm of ψ_ℓ^n as $\|\psi_\ell^n\|_{l^2} = (h^2\sum_{j=0}^{N-1}\sum_{k=0}^{N-1}|\psi_{\ell,jk}^n|^2)^{\frac{1}{2}}$.

Lemma 3 *(Stability). The compact splitting Fourier spectral method is unconditionally stable. In fact, for every mesh size and time step size $\tau > 0$, we have*

$$\sum_{\ell=-1}^{1}\|\psi_\ell^n\|_{l^2}^2 = \sum_{\ell=-1}^{1}\|\psi_\ell^0\|_{l^2}^2.$$

In other words, the mass is conserved at discrete level.

Proof. For the nonlinear subproblem (3.16) and (3.17), due to $(\mathcal{B}^n)^{\mathsf{H}} = \mathcal{B}^n$, we have

$$\|\Psi^{n+1}\|_{l^2}^2 = \|e^{-i\mathcal{B}^n\tau}\Psi^n\|_{l^2}^2 = \|\Psi^n\|_{l^2}^2, \quad \text{where} \quad \|\Psi^n\|_{l^2}^2 := \sum_{\ell=-1}^{1} \|\psi_\ell^n\|_{l^2}^2.$$

For the evaluation of linear subproblem, we only require to consider (3.14) and (3.9). For (3.14), applying the subsequent identities

$$\sum_{q=-N/2}^{N/2-1} e^{i2\pi jq/N} = \sum_{q=0}^{N-1} e^{i2\pi jq/N} = \begin{cases} 0, & j \neq mN, \\ N, & j = mN, \end{cases} \quad m \in \mathbb{Z}, \tag{3.18}$$

we obtain

$$\begin{aligned}\|\phi_\ell^{(1)}\|_{l^2}^2 &= h^2 \sum_{j=0}^{N-1}\sum_{k=0}^{N-1} |\phi_{\ell,jk}^{(1)}|^2 = h^2 N \sum_{k=0}^{N-1}\sum_{p=-N/2}^{N/2-1} \left| e^{ia_1 y_k v_p^x} \left(\widehat{\psi_\ell^n(\cdot, y_k)}\right)_p \right|^2 \\ &= h^2 N \sum_{k=0}^{N-1}\sum_{p=-N/2}^{N/2-1} \left| \left(\widehat{\psi_\ell^n(\cdot, y_k)}\right)_p \right|^2 = h^2 \sum_{j=0}^{N-1}\sum_{k=0}^{N-1} |\psi_{\ell,jk}^n|^2 = \|\psi_\ell^n\|_{l^2}^2.\end{aligned}$$

In a similar way, we have the following equalities

$$\|\phi_\ell^n\|_{l^2}^2 = \|\phi_\ell^{(2)}\|_{l^2}^2 = \|\phi_\ell^{(1)}\|_{l^2}^2 = \|\psi_\ell^n\|_{l^2}^2. \tag{3.19}$$

For (3.9), by using (3.18) and $W^{\mathsf{H}}W = I_3$, we obtain

$$\begin{aligned}\|\Phi^{n+1}\|_{l^2}^2 &= h^2 N^2 \sum_{(p,q)\in\mathcal{T}_N} \left| e^{-\frac{1}{2}i[(v_p^x)^2+(v_q^y)^2]\tau} \, W(t_{n+1}) \, (\widehat{\Phi^n})_{pq} \right|^2 \\ &= h^2 N^2 \sum_{(p,q)\in\mathcal{T}_N} \left| (\widehat{\Phi^n})_{pq} \right|^2 = \|\Phi^n\|_{l^2}^2.\end{aligned} \tag{3.20}$$

Through the above discussion, we have the following conclusion

$$\sum_{\ell=-1}^{1} \|\psi_\ell^{n+1}\|_{l^2}^2 = \sum_{\ell=-1}^{1} \|\phi_\ell^{n+1}\|_{l^2}^2 = \sum_{\ell=-1}^{1} \|\phi_\ell^n\|_{l^2}^2 = \sum_{\ell=-1}^{1} \|\psi_\ell^n\|_{l^2}^2.$$

Then the proof is completed. □

Lemma 4 *(Magnetization conservation). The magnetization $\mathcal{M}(\Psi)$ is conserved at discrete level when $\gamma = 0$. In fact, for every mesh size and time step size $\tau > 0$, we have*

$$\sum_{\ell=-1}^{1} \ell \|\psi_\ell^n\|_{l^2}^2 = \sum_{\ell=-1}^{1} \ell \|\psi_\ell^0\|_{l^2}^2.$$

Proof. For the linear subproblem, we know that $W(t) = I_3$ when $\gamma = 0$. Therefore, from (3.19)-(3.20), we obtain

$$\|\psi_\ell^{n+1}\|_{l^2}^2 = \|\psi_\ell^n\|_{l^2}^2, \quad \ell = 1, 0, -1.$$

For the nonlinear subproblem (3.17), a direct computation shows

$$\begin{aligned}|\psi_1^{n+1}|^2 - |\psi_{-1}^{n+1}|^2 &= \cos^2(c_1\tau|\mathbf{F}^n|)\left(|\psi_1^n|^2 - |\psi_{-1}^n|^2\right) \\ &\quad + \frac{\sin^2(c_1\tau|\mathbf{F}^n|)}{|\mathbf{F}^n|^2}\left(\left|F_z^n\psi_1^n + \frac{1}{\sqrt{2}}F_-^n\psi_0^n\right|^2 - \left|\frac{1}{\sqrt{2}}F_+^n\psi_0^n - F_z^n\psi_{-1}^n\right|^2\right) \\ &= \cos^2(c_1\tau|\mathbf{F}^n|)\left(|\psi_1^n|^2 - |\psi_{-1}^n|^2\right) + \frac{\sin^2(c_1\tau|\mathbf{F}^n|)}{|\mathbf{F}^n|^2}|\mathbf{F}^n|^2\left(|\psi_1^n|^2 - |\psi_{-1}^n|^2\right) \\ &= |\psi_1^n|^2 - |\psi_{-1}^n|^2.\end{aligned}$$

So we have $\|\psi_1^{n+1}\|_{l^2}^2 - \|\psi_{-1}^{n+1}\|_{l^2}^2 = \|\psi_1^n\|_{l^2}^2 - \|\psi_1^n\|_{l^2}^2$. The proof is completed. □

4. Numerical results

Here, we first conduct the spatial/temporal accuracies confirmation and efficiency test. Then, we explore the dynamical laws, including the conservation of mass, energy and magnetization, along with the evolution of condensate widths and angular momentum

Table 2
Numerical errors of CmpStrang and CmpYoshida at time $t = 0.5$ for 2D case in Example 2.

CmpStrang	**Temporal** direction				
	τ	1/80	1/160	1/320	1/640
	$e_1^{h_0,\tau}$	1.1681E-03	2.9159E-04	7.2870E-05	1.8216E-05
	rate		2.0022	2.0005	2.0001
	$e_0^{h_0,\tau}$	5.0694E-04	1.2672E-04	3.1680E-05	7.9199E-06
	rate		2.0001	2.0000	2.0000
	$e_{-1}^{h_0,\tau}$	1.1520E-03	2.8756E-04	7.1863E-05	1.7964E-05
	rate		2.0022	2.0005	2.0001
	Spatial direction				
	h	1/2	1/4	1/8	1/16
	e_1^{h,τ_0}	2.8072E-01	4.3046E-03	5.5245E-08	1.2753E-12
	e_0^{h,τ_0}	1.6902E-01	2.2335E-03	2.3224E-08	1.2208E-12
	e_{-1}^{h,τ_0}	2.9152E-01	4.5147E-03	5.7187E-08	1.3704E-12
CmpYoshida	**Temporal** direction				
	τ	1/80	1/160	1/320	1/640
	$e_1^{h_0,\tau}$	5.6905E-05	3.6223E-06	2.2751E-07	1.4237E-08
	rate		3.9736	3.9929	3.9982
	$e_0^{h_0,\tau}$	1.7442E-05	1.1126E-06	6.9922E-08	4.3767E-09
	rate		3.9706	3.9920	3.9978
	$e_{-1}^{h_0,\tau}$	5.6046E-05	3.5675E-06	2.2407E-07	1.4021E-08
	rate		3.9736	3.9929	3.9982
	Spatial direction				
	h	1/2	1/4	1/8	1/16
	e_1^{h,τ_0}	6.4844E-02	1.8722E-04	1.5849E-09	1.6546E-12
	e_0^{h,τ_0}	1.6902E-01	2.2335E-03	2.3224E-08	3.5761E-12
	e_{-1}^{h,τ_0}	2.9152E-01	4.5149E-03	5.7187E-08	3.6449E-12

expectation. Finally, we apply our method to investigate some interesting phenomena, such as the effect of SOC on dynamics and the dynamics of quantized vortices.

4.1. Accuracy confirmation

Here, we test the spatial and temporal accuracies in both 2D and 3D. For convenience, we denote the second-order Fourier spectral method based on Strang splitting as **CmpStrang**, and the fourth-order method based on Yoshida scheme as **CmpYoshida**. The numerical errors are computed as

$$e_\ell^{h,\tau} := \|\psi_\ell^{\mathrm{ref}} - \psi_\ell^{(h,\tau)}\|_{l^2} \ / \ \|\psi_\ell^{\mathrm{ref}}\|_{l^2}, \qquad \ell = 1, 0, -1,$$

where ψ_ℓ^{ref} denotes the reference solution, and $\psi_\ell^{(h,\tau)}$ denotes the numerical result obtained with the mesh size h and time step τ.

To confirm the temporal convergence, we compute the wave function with a small mesh size $h_0 = \frac{1}{2^{7-d}}$, and the reference solution ψ_ℓ^{ref} is obtained by CmpYoshida with mesh size h_0 and a small time step $\tau_0 = 10^{-4}$. To confirm the spatial convergence, we compute the wave function with different mesh size h and the reference solution is obtained by CmpStrang/CmpYoshida with h_0 and τ_0.

Example 2 *(Accuracy)*. Here, we test the spatial and temporal accuracies for both 2D and 3D cases. To this end, we choose the harmonic potential $V(\mathbf{x}) = |\mathbf{x}|^2/2$, $\Omega = 0.2$ and the following parameters

- **2D case**: $c_0 = 100,\ c_1 = -1,\ \gamma = 0.3$.
- **3D case**: $c_0 = 10,\ c_1 = 1,\ \gamma = 0.1$.

The initial data is chosen as

$$\psi_1^0(\mathbf{x}) = \phi(\mathbf{x}), \qquad \psi_0^0(\mathbf{x}) = 3\sqrt{2}\phi(\mathbf{x}), \qquad \psi_{-1}^0(\mathbf{x}) = \phi(\mathbf{x}), \tag{4.1}$$

where $\phi(\mathbf{x}) = \sqrt{0.05/\pi}e^{-|\mathbf{x}|^2/2}$ for 2D case and $\phi(\mathbf{x}) = \sqrt{0.05}/\pi^{3/4}e^{-|\mathbf{x}|^2/2}$ for 3D case.

Table 2 presents the temporal and spatial errors of CmpStrang and CmpYoshida at time $t = 0.5$ on the computational domain $\mathcal{D} = [-12, 12]^2$ for the 2D case, while Table 3 shows those at time $t = 0.3$ on $[-8, 8]^3$ for the 3D case. From Tables 2-3, we can conclude

Table 3
Numerical errors of CmpStrang and CmpYoshida at time $t = 0.3$ for 3D case in Example 2.

CmpStrang	**Temporal** direction				
	τ	1/40	1/80	1/160	1/320
	$e_1^{h_0,\tau}$	1.0786E-04	2.6946E-05	6.7353E-06	1.6837E-06
	rate		2.0010	2.0002	2.0001
	$e_0^{h_0,\tau}$	8.8380E-05	2.2080E-05	5.5191E-06	1.3797E-06
	rate		2.0010	2.0002	2.0001
	$e_{-1}^{h_0,\tau}$	1.0755E-04	2.6869E-05	6.7160E-06	1.6789E-06
	rate		2.0010	2.0002	2.0001
	Spatial direction				
	h	1	1/2	1/4	1/8
	e_1^{h,τ_0}	2.2081E-02	2.6570E-04	2.3092E-09	5.6024E-13
	e_0^{h,τ_0}	1.7534E-02	1.8530E-04	1.4885E-09	5.4151E-13
	e_{-1}^{h,τ_0}	2.3009E-02	2.7258E-04	2.4044E-09	4.3450E-13
CmpYoshida	**Temporal** direction				
	τ	1/20	1/40	1/80	1/160
	$e_1^{h_0,\tau}$	1.2173E-06	7.8463E-08	4.9435E-09	3.0974E-10
	rate		3.9555	3.9884	3.9964
	$e_0^{h_0,\tau}$	9.9441E-07	6.4016E-08	4.0318E-09	2.5257E-10
	rate		3.9574	3.9889	3.9967
	$e_{-1}^{h_0,\tau}$	1.2168E-06	7.8428E-08	4.9411E-09	3.0951E-10
	rate		3.9556	3.9885	3.9968
	Spatial direction				
	h	1	1/2	1/4	1/8
	e_1^{h,τ_0}	2.2081E-02	2.6570E-04	2.3092E-09	1.6691E-12
	e_0^{h,τ_0}	1.7534E-02	1.8530E-04	1.4885E-09	1.6216E-12
	e_{-1}^{h,τ_0}	2.3009E-02	2.7258E-04	2.4044E-09	1.5942E-12

Table 4
Timing results (in seconds) of CmpStrang and CmpYoshida versus the total grid number N_{tot} for d-dimensional problems in Example 3.

	N_{tot}	64^d	128^d	192^d	256^d
$d = 2$	CmpStrang	0.27	1.3	2.8	5.5
	CmpYoshida	0.76	3.4	7.8	14.8
$d = 3$	CmpStrang	24	226	786	1928
	CmpYoshida	62	610	2108	5392

that CmpStrang/CmpYoshida is *second/fourth* order accurate in time and *spectrally* accurate in space. A higher order operator splitting scheme is easy to construct since both subproblems can be exactly integrated.

4.2. Efficiency test

Since there is no other method ever been proposed for such system, we choose to show the efficiency performance by investigating the computational costs, in terms of computational time, as a function of the discrete problem size. Similar efficiency demonstration about RSDA part was studied by a comparison with NUFFT-accelerated Fourier spectral interpolation in earlier subsection 3.1.2.

Example 3 *(Efficiency)*. Here, we explore the relationship between computational time and total grid number $N_{tot} := N^d$. To this end, we choose the harmonic potential $V(\mathbf{x}) = |\mathbf{x}|^2/2$, $\Omega = 0.2$, $c_0 = 10$, $c_1 = 1$, $\gamma = 0.1$ and the initial data (4.1). The algorithms were implemented in FORTRAN, and run on a single 2.30GH Intel(R) Xeon(R) Sliver 4316 CPU with a 30 MB cache in Ubuntu GNU/Linux with the Intel complier ifort.

Table 4 and Fig. 1 present the computational time (in seconds), elapsed from $t = 0$ to $t = 0.1$ with time step $\tau = 10^{-3}$, as a function of the total grid number N_{tot} in both 2D and 3D problems. From Table 4 and Fig. 1, we can conclude that our method is efficient and the CPU time scales approximately as $CN_{tot}\log(N_{tot})$, which is consistent with our theoretical analysis (Remark 3.5).

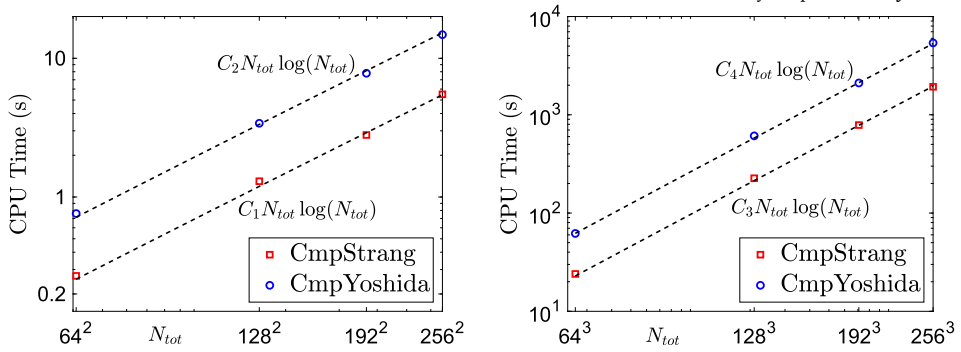

Fig. 1. Log-log plots of timing results for CmpStrang and CmpYoshida versus the total grid number N_{tot} for both $2D$ (left) and $3D$ (right) problems in Example 3.

Table 5
Number of one-dimensional FFT/iFFT operators per time step for CmpStrang/CmpYoshida and ADIStrang/ADIYoshida methods in Example 4.

	Order	Method	Number of FFT/iFFT pairs
2D	Second	CmpStrang	$18N$
		ADIStrang	$12N$
	Fourth	CmpYoshida	$54N$
		ADIYoshida	$63N$
3D	Second	CmpStrang	$21N^2$
		ADIStrang	$24N^2$
	Fourth	CmpYoshida	$63N^2$
		ADIYoshida	$126N^2$

4.3. Comparisons with non-compact splitting

In this subsection, we compare our method with other non-compact splitting method. As shown in [28], compact splitting provides a more straightforward framework for constructing high-order schemes. We conduct a comprehensive comparison in terms of accuracy and efficiency. Since no other method has ever been proposed, we choose to adapt the classical Alternating Direction Implicit (ADI) technique, which has been successfully applied to rotating BECs without SOC term. To be specific, we split the Hamiltonian into three parts, that is, nonlinear part and the other two parts derived by applying ADI to the linear part. Take the 2D case as an example, we split the linear operator $\mathcal{A}$ (1.7) into two parts, i.e., $\mathcal{A} = \mathcal{A}_1 + \mathcal{A}_2$, where

$$\mathcal{A}_1 = (-\frac{1}{2}\partial_{xx} - \Omega i y\partial_x)I_3 - \gamma\begin{pmatrix} 0 & i\partial_x & 0 \\ i\partial_x & 0 & i\partial_x \\ 0 & i\partial_x & 0 \end{pmatrix}$$

and

$$\mathcal{A}_2 = (-\frac{1}{2}\partial_{yy} + \Omega i x\partial_y)I_3 - \gamma\begin{pmatrix} 0 & \partial_y & 0 \\ -\partial_y & 0 & \partial_y \\ 0 & -\partial_y & 0 \end{pmatrix}.$$

Each of the above subproblem can be exactly integrated in Fourier space. For convenience, we denote the second-order Fourier spectral method based on Strang splitting as **ADIStrang** and the fourth-order method based on the Yoshida scheme as **ADIYoshida**.

Example 4 *(Comparison of CmpStrang/CmpYoshida and ADIStrang/ADIYoshida).* Here, we compare CmpStrang/CmpYoshida with ADIStrang/ADIYoshida methods in terms of accuracy and efficiency. To this end, we choose the harmonic potential $V(\mathbf{x}) = |\mathbf{x}|^2/2$, $\Omega = 0.95$, $c_0 = 10$, $c_1 = 1$ and $\gamma = 5$. The initial data is chosen as (4.1).

Fig. 2 and Table 5 present the accuracy and efficiency (measured by the number of FFT/iFFT operations) of the CmpStrang/CmpYoshida and ADIStrang/ADIYoshida methods. From these results, it is evident that our method achieves better accuracy. Except for the second-order ADIStrang scheme in 2D, our method exhibits superior efficiency. Moreover, the advantages of our method become more prominent as the convergence order increases. Therefore, we can conclude that the compact splitting method offers a significant advantage in constructing high-order schemes.

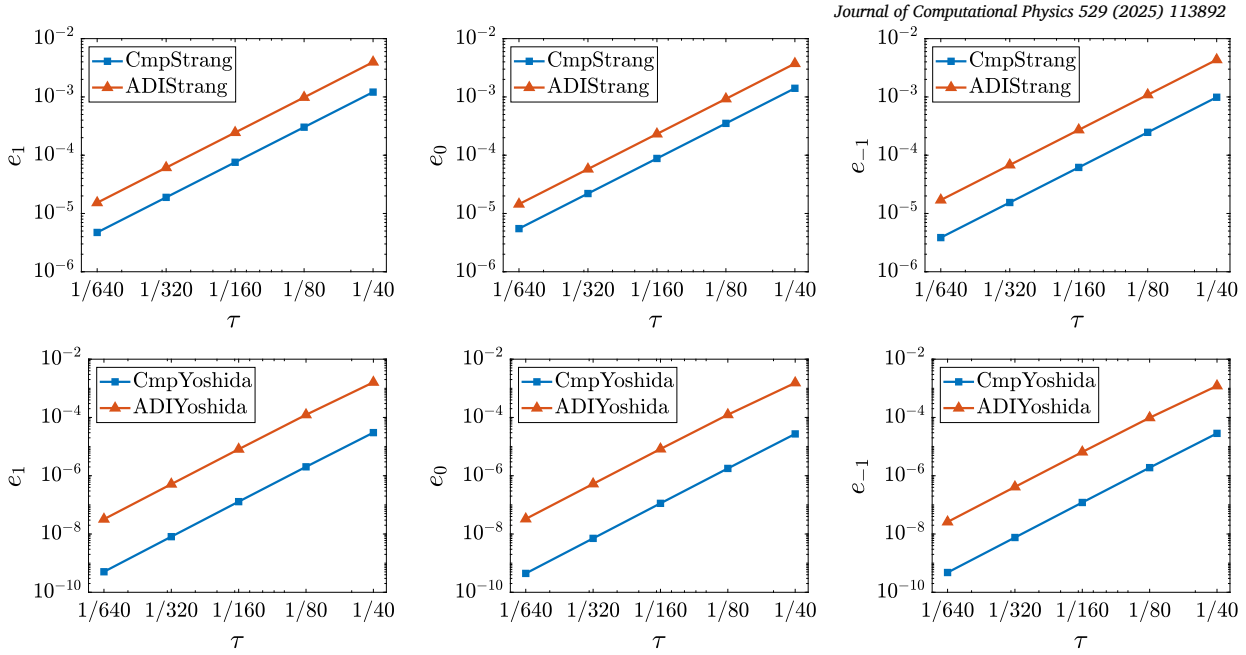

Fig. 2. Comparison of accuracy between CmpStrang/CmpYoshida and ADIStrang/ADIYoshida methods in Example 4.

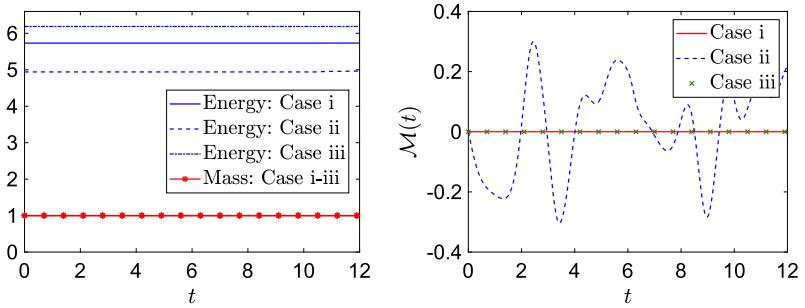

Fig. 3. Evolution of energy $\mathcal{E}(t)$ and mass $\mathcal{N}(t)$ (left) and magnetization $\mathcal{M}(t)$ (right) for Case i-Case iii in Example 5.

4.4. Dynamical properties verification

Here, we investigate the dynamical laws, focusing on the conservation of mass, energy and magnetization, as well as the evolution of condensate widths and angular momentum expectation.

Example 5. Here, we consider the 2D case, and the initial condition is the same as (4.1) with $\phi(\mathbf{x}) = \sqrt{0.05/\pi}e^{-|\mathbf{x}|^2/2}(x+iy)$. We take $\Omega = 0.2$ and study the following three cases

- **Case i**: $\gamma_x = \gamma_y = 1$, $\gamma = 0$, $c_0 = 100$, $c_1 = -1$.
- **Case ii**: $\gamma_x = \gamma_y = 1$, $\gamma = 1$, $c_0 = 80$, $c_1 = 0.8$.
- **Case iii**: $\gamma_x = 1$, $\gamma_y = 1.4$, $\gamma = 0$, $c_0 = 100$, $c_1 = -1$.

The computational domain, mesh size and time step are respectively taken as $D = [-16, 16]^2$, $h = 1/8$ and $\tau = 10^{-3}$.

In Fig. 3, we present the dynamics of energy $\mathcal{E}(t)$, mass $\mathcal{N}(t)$ and magnetization $\mathcal{M}(t)$ computed numerically from the CGPEs over the interval $t \in [0, 12]$. We find that our method conserves the mass and magnetization (when $\gamma = 0$) very well during the dynamics. Fig. 4 shows that if the external trap is radically symmetric and $\gamma = 0$, the angular momentum expectation is conserved and condensate width δ_r is periodic. Furthermore, we observe that $\delta_x(t) = \delta_y(t) = \frac{1}{2}\delta_r(t)$ for radially symmetric initial data. These numerical observations are consistent with the analytical results.

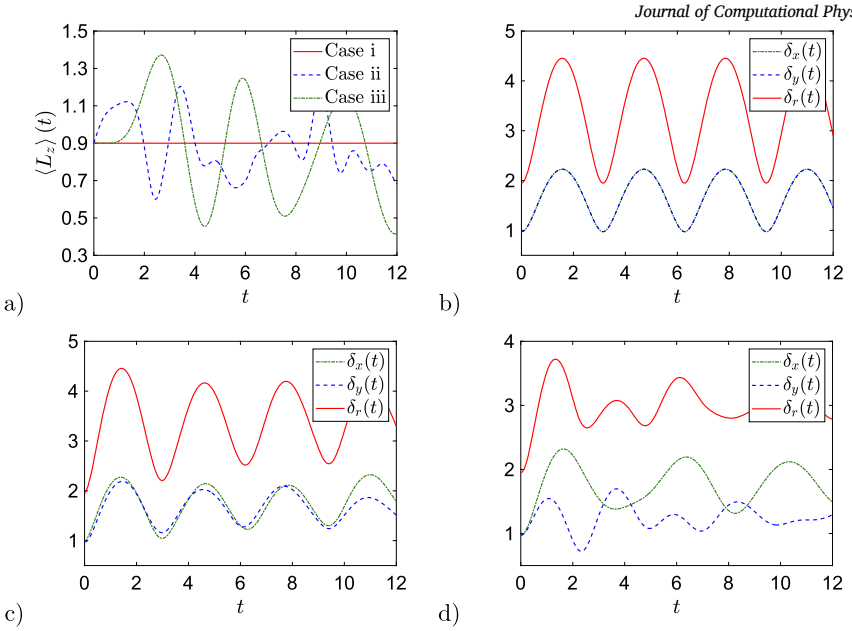

Fig. 4. Evolution of angular momentum expectation $\langle L_z \rangle(t)$ (a) and condensate widths (b)-(d) for Case i-Case iii in Example 5.

4.5. SOC effects

In this subsection, we study the effects of SOC on dynamics in rotating SOC spin-1 BECs.

Example 6. In our simulation, the parameters are chosen as $\Omega = 0.4,\ \gamma_x = \gamma_y = 1,\ c_0 = 100,\ c_1 = -1$ and different $\gamma = 0, 0.7, 2$. We consider the following two cases with different initial data

- **Case i**: $\psi_1^0(\mathbf{x}) = \phi(\mathbf{x}),\ \ \psi_0^0(\mathbf{x}) = 3\sqrt{2}\phi(\mathbf{x}),\ \ \psi_{-1}^0(\mathbf{x}) = \phi(\mathbf{x})$.
- **Case ii**: $\psi_1^0(\mathbf{x}) = \phi(\mathbf{x}),\ \psi_0^0(\mathbf{x}) = 3\sqrt{2}\phi(\mathbf{x})(x + iy),\ \psi_{-1}^0(\mathbf{x}) = \phi(\mathbf{x})$,

where $\phi(\mathbf{x}) = \sqrt{0.05/\pi}e^{-|\mathbf{x}|^2}$.

In practice, we choose the computational domain $\mathcal{D} = [-16, 16]^2$, mesh size $h = 1/16$ and time step $\tau = 10^{-3}$. Figs. 5 and 6 depict contour plots of the densities at time $t = 1$ with different γ for Case i-Case ii respectively. From these figures, we can see that spin-orbit coupling interaction can generate spatial spin structures [17].

4.6. Dynamics of quantized vortices

In the following, we study the dynamics of quantized vortices in rotating SOC spin-1 BECs.

Example 7. Here, we choose $d = 2$, $c_0 = 100$, $c_1 = -1$, $\Omega = 0.7$ and $\gamma = 0.4$. The trapping potential is choose as the harmonic one (1.5) with $\gamma_x = \gamma_y = 1$. The initial data is chosen as a stationary vortex state computed by the preconditioned conjugate gradient method [27] for the chosen parameters. The dynamics of vortices are studied for the following two cases

- **Case i**: perturb the spin-orbit coupling by setting $\gamma = 0.8$.
- **Case ii**: perturb the external potential by setting $\gamma_x = 1.05$, $\gamma_y = 0.95$.

In our simulations, we take $\mathcal{D} = [-10, 10]^2$, $N = 256$ and $\tau = 10^{-3}$. Figs. 7-8 present the contour plots of the densities $|\psi_{\ell'}|^2$ computed by CmpYoshida at different times for Case i and Case ii. We see that during the dynamics, the vortices rotate to form different patterns because of spin-orbit coupling interaction in Case i and the anisotropic external potential in Case ii. In addition, the results in Case ii are similar to those obtained in single-component BEC [6], where the anisotropic compression of the vortex was observed due to the anisotropic external potential.

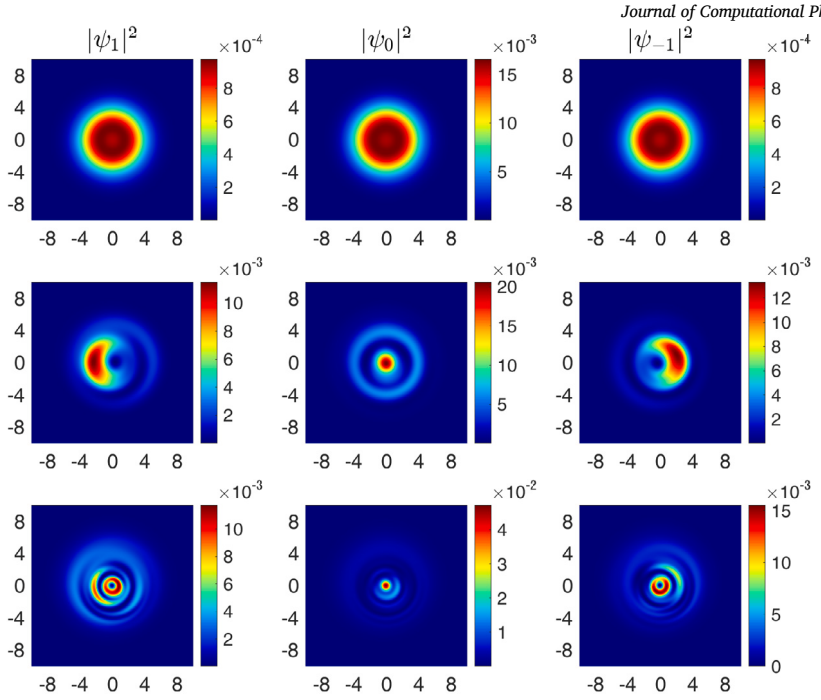

Fig. 5. Contour plots of the densities with $\gamma = 0, 0.7, 2$ (top to bottom) in Case i of Example 6. (For interpretation of the colors in the figure(s), the reader is referred to the web version of this article.)

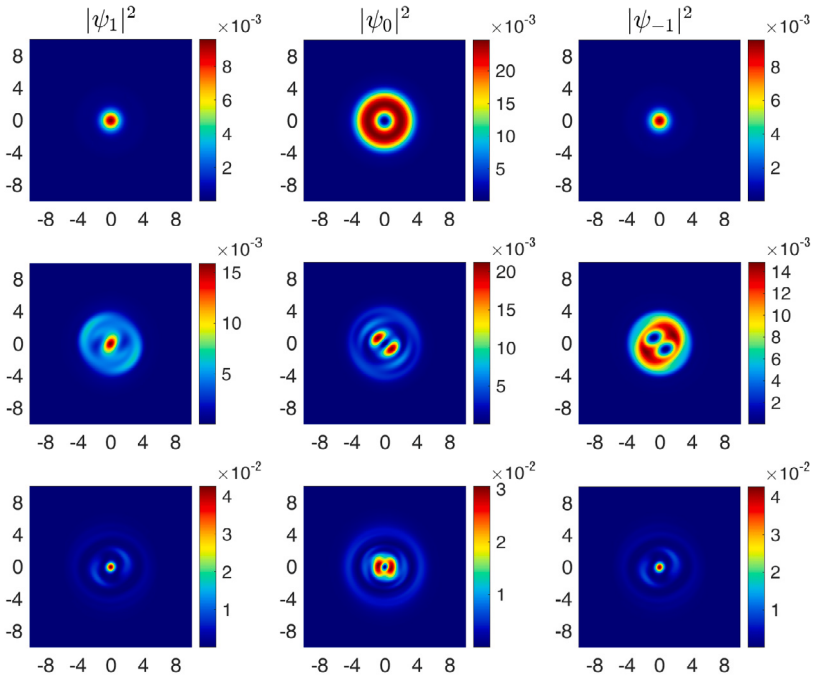

Fig. 6. Contour plots of the densities with $\gamma = 0, 0.7, 2$ (top to bottom) in Case ii of Example 6.

5. Conclusions

We proposed efficient high-order numerical schemes to simulate the dynamics of rotating SOC spin-1 BECs. The Hamiltonian is split into the linear part, including the Laplace, rotation and SOC terms, and the nonlinear part (the remaining terms). The nonlinear subproblem is integrated analytically in physical space as usual. Importantly, we integrate the linear subproblem exactly and explicitly in phase space by mapping the wave function through a rotation of variables and using a time-dependent matrix decomposition. This

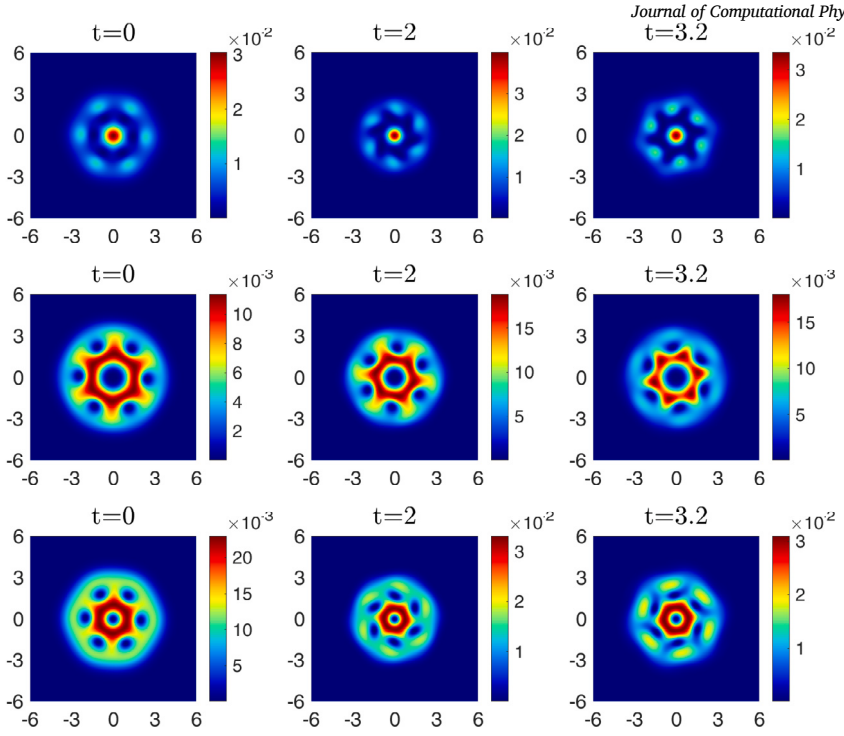

Fig. 7. Contour plots of $|\psi_\ell|^2$ ($\ell = 1, 0, -1$, from top to bottom) for Case i in Example 7.

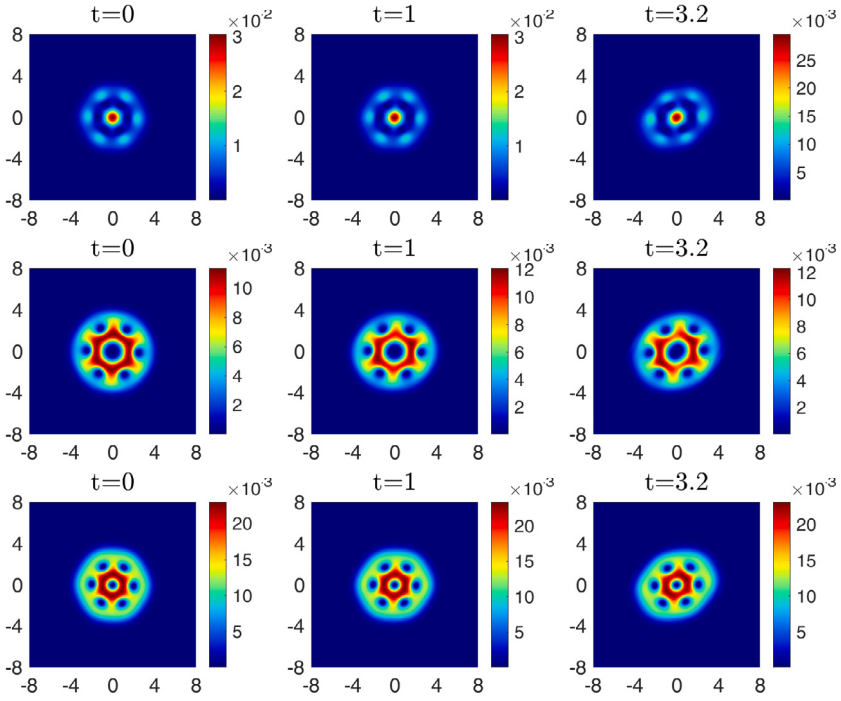

Fig. 8. Contour plots of $|\psi_\ell|^2$ ($\ell = 1, 0, -1$, from top to bottom) for Case ii in Example 7.

compact splitting facilitates the design of high-order Fourier spectral method. All the calculations, including the function-rotation mapping and the Fourier spectral method, are implemented on a fixed rectangular domain in the original Cartesian coordinates with purely FFT/iFFT, thus achieving almost optimal efficiency. Our method is spectrally accurate in space and high order in time. It is explicit, unconditionally stable, and conserves the mass and magnetization (when $\gamma = 0$) at discrete level. The dynamical laws of total mass, energy, magnetization, angular momentum expectation and condensate widths are also derived and confirmed numerically.

Moreover, our method can be easily adapted and extended to simulate more general rotating systems, such as the rotating SOC spin-F BECs with/without dipole-dipole interactions.

CRediT authorship contribution statement

Xin Liu: Writing – review & editing, Writing – original draft, Visualization, Methodology, Formal analysis, Data curation. **Yongjun Yuan:** Writing – review & editing, Project administration, Formal analysis, Conceptualization. **Yong Zhang:** Writing – review & editing, Supervision, Project administration, Methodology, Funding acquisition, Formal analysis.

Declaration of competing interest

The authors declare the following financial interests/personal relationships which may be considered as potential competing interests: Yongjun Yuan reports financial support was provided by the National Natural Science Foundation of China (No. 12471375). Xin Liu and Yong Zhang report financial support was provided by the National Natural Science Foundation of China (No. 12271400) and the National Key R&D Program of China (No. 2024YFA1012803). Yong Zhang also reports financial support was provided by Yunnan Key Laboratory of Modern Analytical Mathematics and Applications (No. 202302AN360007). If there are other authors, they declare that they have no known competing financial interests or personal relationships that could have appeared to influence the work reported in this paper.

Acknowledgements

This work was partially supported by the National Natural Science Foundation of China No. 12471375 (Y. Yuan), No. 12271400, the National Key R&D Program of China No. 2024YFA1012803 (X. Liu and Y. Zhang), and partially supported by Yunnan Key Laboratory of Modern Analytical Mathematics and Applications No. 202302AN360007 while the third author was visiting Yunnan Normal University.

Appendix A. Proof of Lemma 1

Proof. Using (1.6) and integration by parts, after a simple calculation, we have

$$\begin{aligned}\frac{d\langle L_z\rangle(t)}{dt} &= \sum_{\ell=-1}^{1}\int_{\mathbb{R}^d}\left[(\partial_t\bar{\psi}_\ell)\,(L_z\psi_\ell)+\bar{\psi}_\ell\;L_z(\partial_t\psi_\ell)\right]\mathrm{d}\mathbf{x}\\ &= \int_{\mathbb{R}^d} V(\mathbf{x})(x\partial_y-y\partial_x)\rho-\gamma i\left(\bar{\psi}_1L_0\psi_0+\psi_1L_1\bar{\psi}_0-\bar{\psi}_{-1}L_1\psi_0-\psi_{-1}L_0\bar{\psi}_0\right)\mathrm{d}\mathbf{x}\\ &= (\gamma_x^2-\gamma_y^2)\int_{\mathbb{R}^d} xy\;\rho\;\mathrm{d}\mathbf{x}-2\gamma\Re\int_{\mathbb{R}^d} i\left(\bar{\psi}_1L_0\psi_0-\bar{\psi}_{-1}L_1\psi_0\right)\mathrm{d}\mathbf{x}.\end{aligned}$$

The proof is completed. □

Appendix B. Proof of Lemma 2

Proof. Using (1.6), (2.6) and integration by parts, a simple calculation shows

$$\begin{aligned}\frac{d\delta_{\alpha,1}(t)}{dt} &= \int_{\mathbb{R}^d}\alpha^2\;\partial_t|\psi_1|^2\mathrm{d}\mathbf{x}=\int_{\mathbb{R}^d}\alpha^2\;(\partial_t\psi_1\bar{\psi}_1+\psi_1\partial_t\bar{\psi}_1)\mathrm{d}\mathbf{x}\\ &= 2\Re\int_{\mathbb{R}^d} i\alpha\left[\psi_1\partial_\alpha\bar{\psi}_1-2\Omega|\psi_1|^2L_z\alpha+c_1\alpha\bar{\psi}_0^2\psi_1\psi_{-1}+\gamma\alpha\psi_1L_1\bar{\psi}_0\right]\mathrm{d}\mathbf{x}.\end{aligned}$$

Similarly, we obtain

$$\begin{aligned}\frac{d\delta_{\alpha,0}(t)}{dt} &= 2\Re\int_{\mathbb{R}^d} i\alpha\left[\psi_0\partial_\alpha\bar{\psi}_0-2\Omega|\psi_0|^2L_z\alpha-2c_1\alpha\bar{\psi}_0^2\psi_1\psi_{-1}+\gamma\alpha\left(\psi_0L_1\bar{\psi}_{-1}+\bar{\psi}_0L_1\psi_1\right)\right]\mathrm{d}\mathbf{x}.\\ \frac{d\delta_{\alpha,-1}(t)}{dt} &= 2\Re\int_{\mathbb{R}^d} i\alpha\left[\psi_{-1}\partial_\alpha\bar{\psi}_{-1}-2\Omega|\psi_{-1}|^2L_z\alpha+c_1\alpha\bar{\psi}_0^2\psi_1\psi_{-1}+\gamma\alpha\bar{\psi}_{-1}L_1\psi_0\right]\mathrm{d}\mathbf{x}.\end{aligned}$$

Then, a straightforward rearrangement shows

$$\frac{d\delta_\alpha(t)}{dt}=\sum_{\ell=-1}^{1}\frac{d\delta_{\alpha,\ell}(t)}{dt}=2\Re\int_{\mathbb{R}^d} i\alpha\Big[\sum_{\ell=-1}^{1}\left(\psi_\ell\partial_\alpha\bar\psi_\ell-2\Omega|\psi_\ell|^2L_z\alpha\right)$$
$$+\gamma\alpha\left(\psi_1L_1\bar\psi_0+\bar\psi_0L_1\psi_1+\psi_0L_1\bar\psi_{-1}+\psi_{-1}L_1\bar\psi_0\right)\Big]\mathrm{d}\mathbf{x}.$$

Using integration by parts, we have

$$\int_{\mathbb{R}^d}\alpha^2\psi_1L_1\bar\psi_0\mathrm{d}\mathbf{x}=-\int_{\mathbb{R}^d}\bar\psi_0L_1(\alpha^2\psi_1)\mathrm{d}\mathbf{x}=-\int_{\mathbb{R}^d}\left[\alpha^2\bar\psi_0L_1\psi_1+2\alpha\psi_1\bar\psi_0L_1\alpha\right]\mathrm{d}\mathbf{x}.$$

Hence,

$$\frac{d\delta_\alpha(t)}{dt}=2\Re\int_{\mathbb{R}^d} i\alpha\Big[\sum_{\ell=-1}^{1}\left(\psi_\ell\partial_\alpha\bar\psi_\ell-2\Omega|\psi_\ell|^2L_z\alpha\right)-2\gamma\left(\psi_1\bar\psi_0L_1\alpha+\psi_0\bar\psi_{-1}L_1\alpha\right)\Big]\mathrm{d}\mathbf{x}.$$

We continue to differentiate the above equation with respect to t using the same method. The detailed calculation is not difficult but is too lengthy, so we will only provide some key steps. Some tedious manipulations yield

$$\frac{d^2\delta_\alpha(t)}{dt^2}=-2\gamma_r^2\delta_\alpha(t)+\int_{\mathbb{R}^d}\Big[2\sum_{\ell=-1}^{1}\left|\partial_\alpha\psi_\ell\right|^2+c_0\rho^2+c_1|F_z|^2+c_1|F_+|^2$$
$$-2\gamma\left(\bar\psi_1L_0\psi_0+\bar\psi_0L_0\psi_{-1}+\bar\psi_0L_1\psi_1+\bar\psi_{-1}L_1\psi_0\right)$$
$$+(\partial_y-\partial_x)\alpha\sum_{\ell=-1}^{1}\left(4i\Omega\bar\psi_\ell(x\partial_y+y\partial_x)\psi_\ell+2\Omega^2(x^2-y^2)\left|\psi_\ell\right|^2\right)+G_1(\alpha,\gamma,\Psi)\Big]\mathrm{d}\mathbf{x},$$

where

$$G_1(\alpha,\gamma,\Psi)=4\gamma\Re\Big[\alpha\left[(L_1\bar\psi_{-1}+L_0\bar\psi_1)\partial_\alpha\psi_0-(L_0\psi_0)\partial_\alpha\bar\psi_1-(L_1\psi_0)\partial_\alpha\bar\psi_{-1}\right]+L_1\alpha\Big(\psi_0\partial_\alpha\bar\psi_{-1}$$
$$+\psi_1\partial_\alpha\bar\psi_0-\frac{\Omega}{\sqrt{2}}F_-L_z\alpha+\gamma\left[\alpha\bar\psi_{-1}L_0\psi_{-1}+\alpha\psi_1L_0\bar\psi_1-\left|\psi_0\right|^2L_0\alpha-\psi_1\bar\psi_{-1}L_1\alpha\right]\Big)\Big].$$

Hence, we have

$$\frac{d^2\delta_r(t)}{dt^2}=-4\gamma_r^2\delta_r(t)+4\mathcal{E}\left(\Psi(\cdot,0)\right)+4\Omega\langle L_z\rangle(t)+G\left(\gamma,\Psi\right),\tag{B.1}$$

where

$$G(\gamma,\Psi):=G_1(x,\gamma,\Psi)+G_1(y,\gamma,\Psi)$$
$$=4\gamma\Re\int_{\mathbb{R}^d}\left[\frac{\Omega}{\sqrt{2}}(ix+y)F_++\gamma\left(\rho+|\psi_0|^2-\psi_1L_z\bar\psi_1+\psi_{-1}L_z\bar\psi_{-1}\right)\right]\mathrm{d}\mathbf{x}.$$

As a result, when $\gamma=0$, we have $G(0,\Psi)=0$ and $\langle L_z\rangle(t)\equiv\langle L_z\rangle(0)$. Thus the $\delta_r(t)$ given in (2.8) is the unique solution to second order ODE (B.1) with the initial data $\delta_r(0)=\delta_r^{(0)}$ and $\dot\delta_r(0)=\delta_r^{(1)}$. Furthermore, if $\Psi^0(\mathbf{x})$ is radial symmetric, the solution $\Psi(\mathbf{x},t)$ is also radial symmetric since $\gamma_x=\gamma_y$, which implies that [4,5]

$$\delta_x(t)=\delta_y(t)=\frac{1}{2}\delta_r(t),\quad t\ge0.$$

The proof is completed. □

Data availability

Data will be made available on request.

References

[1] M.H. Anderson, J.R. Ensher, M.R. Matthewa, C.E. Wieman, E.A. Cornell, Observation of Bose-Einstein condensation in a dilute atomic vapor, Science 269 (1995) 198–201.
[2] X. Antoine, A. Levitt, Q. Tang, Efficient spectral computation of the stationary states of rotating Bose-Einstein condensates by preconditioned nonlinear conjugate gradient methods, J. Comput. Phys. 343 (2017) 92–109.
[3] W. Bao, Y. Cai, Mathematical models and numerical methods for spinor Bose-Einstein condensates, Commun. Comput. Phys. 24 (2018) 899–965.
[4] W. Bao, Y. Cai, Mathematical theory and numerical methods for Bose-Einstein condensation, Kinet. Relat. Models 6 (2013) 1–135.

[5] W. Bao, Q. Du, Y. Zhang, Dynamics of rotating Bose-Einstein condensates and its efficient and accurate numerical computation, SIAM J. Appl. Math. 66 (2006) 758–786.
[6] W. Bao, D. Marahrens, Q. Tang, Y. Zhang, A simple and efficient numerical method for computing the dynamics of rotating Bose-Einstein condensates via rotating Lagrangian coordinates, SIAM J. Sci. Comput. 35 (2013) A2671–A2695.
[7] W. Bao, H. Wang, An efficient and spectrally accurate numerical method for computing dynamics of rotating Bose-Einstein condensates, J. Comput. Phys. 217 (2006) 612–626.
[8] W. Bao, Y. Zhang, Dynamical laws of the coupled Gross-Pitaevskii equations for spin-1 Bose-Einstein condensates, Methods Appl. Anal. 17 (2010) 49–80.
[9] J. Bernier, F. Casas, N. Crouseilles, Splitting methods for rotations: application to Vlasov equations, SIAM J. Sci. Comput. 42 (2020) A666–A697.
[10] J. Bernier, N. Crouseilles, Y. Li, Exact splitting methods for kinetic and Schrödinger equations, J. Sci. Comput. 86 (2021) 1–35.
[11] Y. Cai, W. Liu, Efficient and accurate gradient flow methods for computing ground states of spinor Bose-Einstein condensates, J. Comput. Phys. 433 (2021) 110183.
[12] F. Dalfovo, S. Giorgini, L.P. Pitaevskii, S. Stringari, Theory of Bose-Einstein condensation in trapped gases, Rev. Mod. Phys. 71 (1999) 463–512.
[13] K.B. Davis, M.O. Mewes, M.R. Andrews, N.J. van Druten, D.S. Durfee, D.M. Kurn, W. Ketterle, Bose-Einstein condensation in a gas of sodium atoms, Phys. Rev. Lett. 75 (1995) 3969–3973.
[14] L. Greengard, J.Y. Lee, Accelerating the nonuniform fast Fourier transform, SIAM Rev. 46 (2004) 443–454.
[15] M.Z. Hasan, C.L. Kane, Colloquium: topological insulators, Rev. Mod. Phys. 82 (2010) 3045–3067.
[16] A. Ji, W. Liu, J. Song, F. Zhou, Dynamical creation of fractionalized vortices and vortex lattices, Phys. Rev. Lett. 101 (2008) 010402.
[17] Y. Kawaguchi, M. Ueda, Spinor Bose-Einstein condensates, Phys. Rep. 520 (2012) 253–381.
[18] J.D. Koralek, C.P. Weber, J. Orenstein, B.A. Bernevig, S. Zhang, S. Mack, D.D. Awschalom, Emergence of the persistent spin helix in semiconductor quantum wells, Nature 458 (2009) 610–613.
[19] R. Liao, Y. Yu, W. Liu, Tuning the tricritical point with spin-orbit coupling in polarized Fermionic condensates, Phys. Rev. Lett. 108 (2012) 080406.
[20] Y. Lin, K. Jiménez-García, I.B. Spielman, Spin-orbit coupled Bose-Einstein condensate, Nature 471 (2011) 83–86.
[21] X. Liu, X. Meng, Q. Tang, Y. Zhang, High-order compact splitting spectral methods for the rotating spin-1 Bose-Einstein condensates in a magnetic field, submitted for publication.
[22] Z. Ma, Y. Zhang, Z. Zhou, An improved semi-Lagrangian time splitting spectral method for the Schrödinger equation with vector potentials using NUFFT, Appl. Numer. Math. 111 (2017) 144–159.
[23] J. Shen, T. Tang, L. Wang, Spectral Methods: Algorithms, Analysis and Applications, Springer, 2011.
[24] D. Stamper-Kurn, M. Andrews, A. Chikkatur, S. Inouye, H. Miesner, J. Stenger, W. Ketterle, Optical confinement of a Bose-Einstein condensate, Phys. Rev. Lett. 80 (1998) 2027–2030.
[25] L.M. Symes, R.I. McLachlan, P.B. Blakie, Efficient and accurate methods for solving the time-dependent spin-1 Gross-Pitaevskii equation, Phys. Rev. E 93 (2016) 053309.
[26] A. Tanaka, A rotation method for raster image using skew transformation, in: Proceedings IEEE Conference on Computer Vision and Pattern Recognition, 1986, pp. 272–277.
[27] W. Yang, Y. Yuan, Y. Zhang, An accurate and efficient numerical method to compute the ground state of the rotating spin-orbit coupled spin-1 Bose-Einstein condensates, preprint.
[28] H. Yoshida, Construction of higher order symplectic integrators, Phys. Lett. A 150 (1990) 262–268.
[29] Y. Yuan, Z. Xu, Q. Tang, H. Wang, The numerical study of the ground states of spin-1 Bose-Einstein condensates with spin-orbit-coupling, East Asian J. Appl. Math. 8 (2018) 598–610.
[30] D. Zhang, T. Gao, P. Zou, L. Kong, R. Li, X. Shen, X. Chen, S. Peng, M. Zhan, H. Pu, K. Jiang, Ground-state phase diagram of a spin-orbital-angular-momentum coupled Bose-Einstein condensate, Phys. Rev. Lett. 122 (2019) 110402.
[31] X. Zhang, B. Li, S. Zhang, Rotating spin-orbit coupled Bose-Einstein condensates in concentrically coupled annular traps, Laser Phys. 23 (2013) 105501.
[32] X. Zhou, J. Zhou, C. Wu, Vortex structures of rotating spin-orbit-coupled Bose-Einstein condensates, Phys. Rev. A 84 (2011) 063624.